Modeling and Analysis of Plasmonic Terahertz Wave Detector Based on Field Effect Transistor

Kwan Sung Kim

Department of Electrical Engineering

Graduate School of UNIST

2016

Modeling and Analysis of Plasmonic Terahertz Wave Detector Based on Field Effect Transistor

Kwan Sung Kim

Department of Electrical Engineering

Graduate School of UNIST
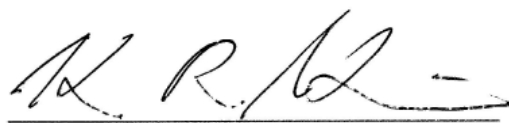
Modeling and Analysis of Plasmonic Terahertz Wave Detector Based on Field Effect Transistor

A thesis

submitted to the Graduate School of UNIST

in partial fulfillment of the

requirements for the degree of

Master of Science

Kwan Sung Kim

1. 21. 2016 of submission

Approved by

_____

Advisor

Kyung Rok Kim

Modeling and Analysis of Plasmonic Terahertz Wave Detector Based on Field Effect Transistor

Kwan Sung Kim

This certifies that the thesis of Kwan Sung Kim is approved.

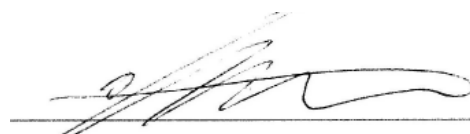1. 21. 2016 of submission

signature

Advisor: Kyung Rok Kim

signature

typed name: Min Suk Kwon

signature

typed name: Jongwon Lee

Abstract

I propose accurate analysis and novel model of the nonresonant plasmonic terahertz (THz) wave detector based on the silicon (Si) field effect transistor (FET) with a technology computer-aided design (TCAD) platform and SPICE simulation. By introducing a quasi-plasma two-dimensional electron gas (2DEG) in the channel of the FET, the physical behavior of the plasma wave has been modeled with the TCAD platform. For accurate analysis of the modulation and propagation of the channel electron density as the plasma wave, I have characterized the quasi-plasma 2DEG model with two key parameters, such as quasi-plasma 2DEG length (l_{QP}) and density (N_{QP}). The l_{QP} and N_{QP} is defined exactly as extracting the average point of the electron density by using the normalization method. Through the quasi-plasma 2DEG modeling, I investigate the performance enhancement of the plasmonic terahertz wave detector based on Si FET according to scaling down the gate oxide thickness (t_{ox}), which is a significant parameter of FET-based plasmonic terahertz detector for the channel electron density modulation. By scaling down t_{ox}, the responsivity (R_v) and noise equivalent power (NEP), which are the important performance metrics of the THz wave detector, have been enhanced. In addition, I report the new NQS compact model for MOSFET-based THz wave detector using SPICE simulation. Because the FETs are intensively considered for THz detector due to their performance and applicability, it is essential to describe the physical behaviors of FET in the THz regime with non-quasi-static (NQS) analysis. However, most of the NQS MOSFET models (e.g., Elmore model) have the complexity of the formulation and fail to describe the device physics for the accurate analysis of fast switching and high-frequency operation. In this work, I have proposed novel NQS compact model of MOSFET, which is applicable for transient simulation of the plasmonic THz detectors. The new SPICE NQS model has been verified by comparing with TCAD device simulation as reference of the complete numerical NQS simulation. For simulation of MOSFET-based plasmonic THz detector with SPICE, I demonstrate the model validity by extracting the photoresponse simulation as the function of the gate voltage at 0.2 THz with the peak point in the sub-threshold region. The proposed novel methodologies will provide the advanced physical analysis and efficient structural design for developing the nonresonant plasmonic terahertz detectors operating in THz regime.

Contents

List of Figures

Figure 3-3. Main procedures of the DC parameter extraction in SPICE.

Figure 3-4. DC Id-Vg simulation results of MOSFET device after matching procedures. The good matching of DC characteristics between TCAD and SPICE has been obtained.

Figure 3-5. Several equivalent MOSFET model for time-varying analysis.

Figure 3-6. Transient simulation result of NQS Elmore model in SPICE at $T_R = 50$ ps.

Figure 3-7. (a) Circuit configuration of new NQS compact model of MOSFET with the lumped circuit elements. (b) Transient simulation results of new NQS compact model of MOSFET with TCAD-based verification.

Figure 3-8. (a) The applied asymmetric boundary condition in simulation results of the new SPICE NQS MOSFET model by adding the various gate-to-drain capacitance C_{gd}. (b) Comparison of the drain voltage amplitude between TCAD and SPICE simulation results according to increase of C_{gd}.

Figure 3-9. Simulation results of the photoresponse as a function of the gate voltage. In accordance with the simplified theory of the nonresonant THz detector, the maximum value of the photoresponse is located in the sub-threshold region ($V_{th} = 0.45$ V).

Figure 5-1. TCAD-based verification of RF simulation results. $V_{gs} = 1.2$ V, $V_{ds} = 1.5$ V [Ref. 53].

Figure 5-2. (a) Experimental results of the photoresponse when the input voltage is applied. (b) Block diagram of the input gate voltage and output photoresponse. By integrating the external gate capacitance, the parasitic capacitance will be eliminated and intrinsic delay time of the THz detector can be estimated.

List of Tables

Nomenclature

AC	Alternating current
BSIM	Berkeley short channel IFGET model
CMOS	Complementary metal-oxide-semiconductor
DC	Direct current
DFG	Difference frequency generator
EM	Electromagnetic
FET	Field effect transistor
FPA	Focal plane array
HBT	Hetero bipolar transistor
LDD	Lightly doped drain
MOSFET	Metal-oxide-semiconductor field effect transistor
NEP	Noise equivalent power
NQS	Non-quasi-static
PWT	Plasma wave transistor
QS	Quasi-static
RF	Radio frequency
RTD	Resonant tunneling diode
SBD	Schottky barrier diode
Si	Silicon
SPICE	Simulation program with integrated circuit emphasis
SSW	Subthreshold swing
TCAD	Technology computer-aided program

THz   Terahertz

THz QCL Terahertz quantum cascade laser

UTC-PD Uni-travelling carrier photodiode

2-D   Two-dimensional

2DEG   Two-dimensional electron gas

Chapter 1

Introduction

1.1 Terahertz Wave and Applications

Terahertz (THz) wave, which is the electromagnetic (EM) wave with a frequency range of 0.1–10 THz, forms the THz gap between the millimeter-wave band developed by the electronics and the far-infrared band developed by the photonics. Because of the distinguished characteristics of THz wave such as good permeability (penetrability) and harmlessness to human body owing to its relatively long wavelength and low energy, the research on the radiation and detection of the THz wave has been intensively performed in recent year owing to their potential applications in the various fields including communication, spectroscopy and THz imaging technology [1-5]. Especially, THz imaging system for the soft materials such as the human body has been regarded as the most promising application of the THz detectors in near future [6-8]. In spite of the advantages, however, THz imaging application is still immature because of the lack of high performance THz detection technology.
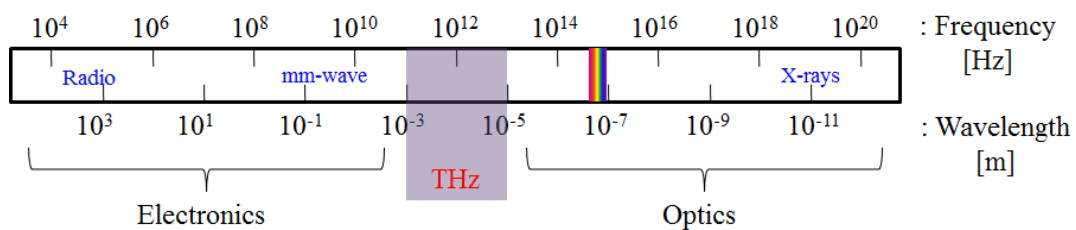
Figure 1-1. Frequency and wavelength of THz wave band (THz gap).
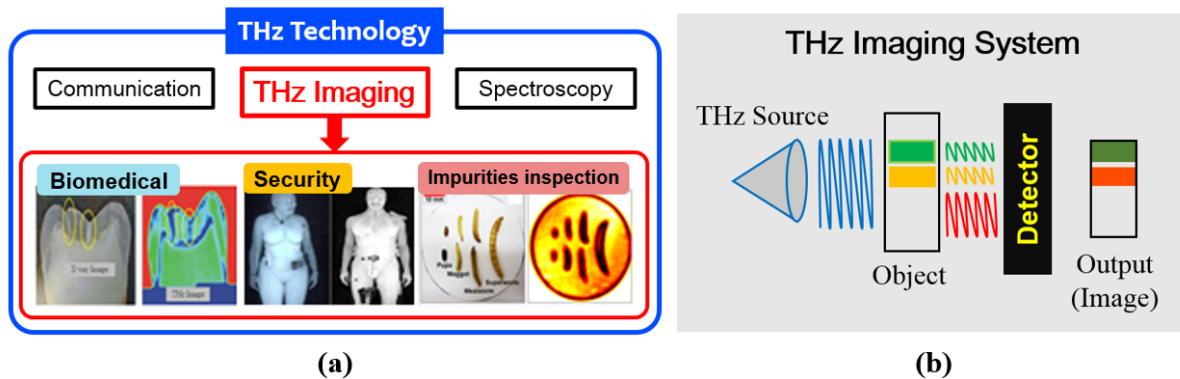
Figure 1-2. (a) THz technology: communication, spectroscopy, and THz imaging. THz imaging such as biomedical, security, impurities inspection is the most promising application of the THz detection in near future

(b) THz imaging system.

THz technology has been developed as aspect of THz photonics (optical engineering) and THz electronics (electronic engineering). It is necessary to achieve the large scale and high output power in THz photonics including optical rectification, difference frequency generator (DFG), terahertz quantum cascade laser (THz QCL), and uni-travelling carrier photodiode (UTC-PD). And in THz electronics such as resonant tunneling diode (RTD) and Schottky barrier diode (SBD), it is needed to obtain the high integration and low output power for small size.

1.2 Plasmonic Terahertz Wave Detector

Nano device technologies have been scaled down to 20 nm for higher operating frequency, however, the operation frequency is limited up to 500 GHz band through the reduction of size in transit mode where drift-diffusion transport of electron depends on cut-off frequency. In case of the transit mode using Schottky barrier diode (SBD) [9] and hetero bipolar transistor (HBT) [10], it is difficult to operate at the THz frequency range. In order to overcome this limitation, plasma wave transistor (PWT), which can operate at more 10 to 100 times electron drift velocity of transit mode, has been used for higher operating frequency. Using the plasma resonance of 2-dimensional (2-D) electron density in channel, the research on THz wave detector incorporating plasma wave has been extensively proceeded owing to work in THz frequency region. As shown in figure 1-3, the operating frequency of the device in plasma mode is much higher than in transit mode.
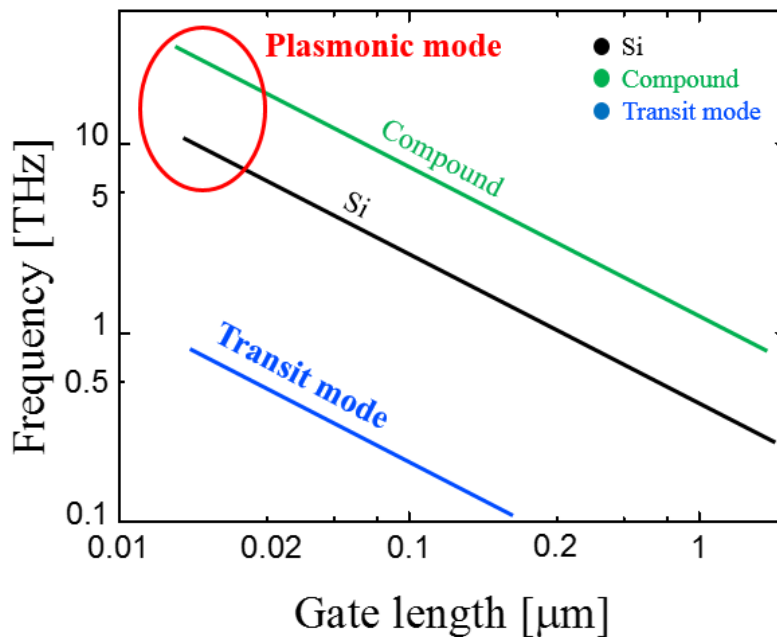
Figure 1-3. Comparison of operation frequency in plasma and transit mode for various semiconductor materials

according to gate length.

1.2.1 Plasma Wave in FETs

Since Dyakonov and Shur have proposed the plasma wave behavior in the channel of the THz detector based on FETs [11, 12], the THz detectors comprising FET devices with two-dimensional electron gas (2DEG) have been reported theoretically [13-15] and experimentally [16]. THz detectors based on field effect transistor (FET), which are more promising than other devices due to their applicability and performance, have been carried out for plasma wave detection in the resonant as well as nonresonant regime by using the silicon (Si) semiconductors [17-21] or III-V compound materials [22-25] such as GaAs/AlGaAs and GaInAs/AlGaAs.

Figure 1-4 shows a description of THz detection mechanism with the 2DEG in FET structure. The detection mechanism occurs due to the nonlinear properties of the 2DEG in the channel region of the field effect transistor (FET), and it leads to the rectification of the AC current by the incoming THz radiation. As a result, a photoresponse arises in the form of a DC voltage difference between the source and drain side of FETs. In order to induce the photoresponse, which forms the DC voltage, the asymmetric condition between the source and the drain should be needed. There are several reasons of such an asymmetry. One of them is the boundary condition difference owing to external capacitances. Another one is the asymmetry in feeding the incoming THz radiation, which can be obtained by using the antenna or by an asymmetric structural design between the source and drain contact pad [26]. And thus, an AC voltage between the source and the gate is induced by the THz radiation. As a result, the asymmetry can arise if a DC current is passed between the source and drain, the asymmetry will create the depletion of the electron near the drain of the channel in FETs.
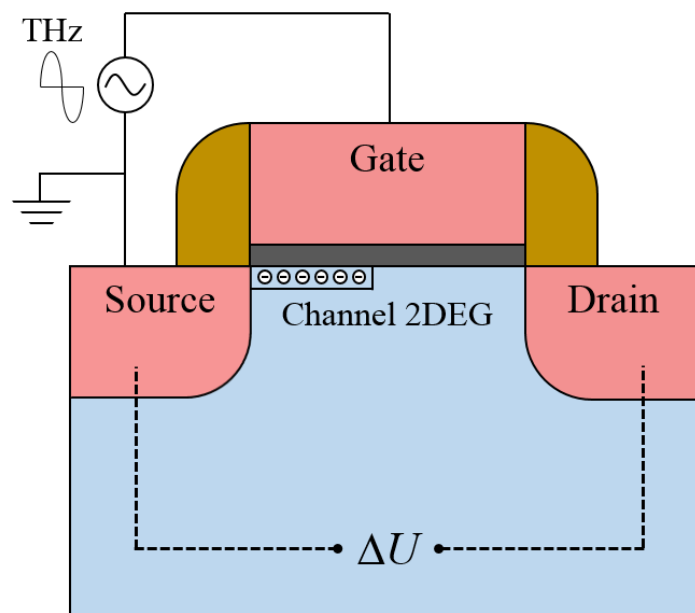
Figure 1-4. Schematic mechanism of THz detector based on channel 2DEG in FET structure.

1.2.2 Operation Principle of Terahertz Detector
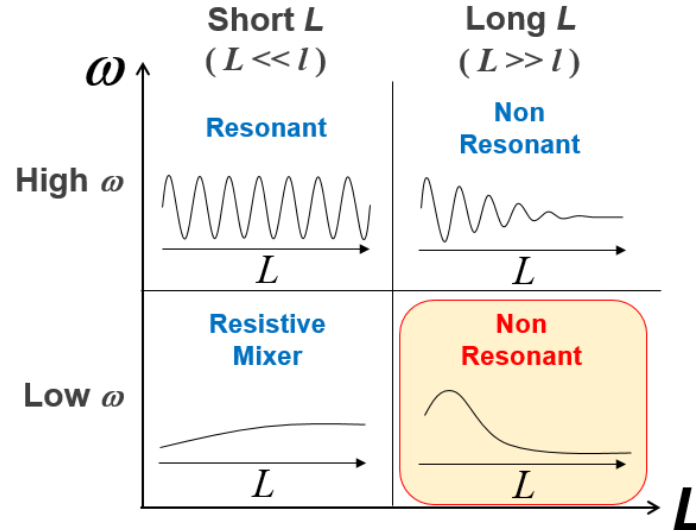
Figure 1-5. Resonant and nonresonant operation of plasma wave in THz region according to the frequency and gate length.

In order to describe the nonlinear properties of the plasma wave as 2DEG in channel region of FET for detection and mixing of the THz wave, the operation of plasma wave in resonant and nonresonant regime should be examined. Figure 1-5 shows operation of the plasma wave in THz frequency region according to the frequency ω and gate length L. The two regimes of the plasma wave operation can be divided depending on the frequency ω, and each of regimes are distinguished into two sub-regimes in accordance with the gate length L [16].

1. High frequency regime ($\omega\tau > 1$)

    The electron momentum relaxation time t determines the electron conductivity $\sigma = ne^2\tau/m$. In this case, the plasma wave in the channel as RLC transmission line can be excited. The plasma wave have a velocity $s = (eU/m)^{1/2}$ and the propagation distance of the plasma wave is $s\tau$.

    a. Short gate ($L < s\tau$)

        The plasma wave in the source side can reach the drain side and reflect, so that the amplitude of the plasma wave is enhanced. In this case, the channel of FET operates as a resonator for plasma wave oscillation

    b. Long gate ($L \gg s\tau$)

        In this case, the plasma wave induced at the source side decays and cannot reach the drain

side of the channel. The AC current exists only at the source side.

2. Low frequency regime ($\omega\tau \ll 1$)

At low frequencies, the plasma wave cannot exist owing to an overdamping. In this case, the properties of operation are determined by the gate length and the parameter $\omega\tau_{RC}$, where τ_{RC} is the RC time constant of the FET.

a. Short gate ($L < (\rho C\omega)^{-1/2}$)

In this case, the AC current flows along with the gate-to-channel capacitance. It operates as the "resistive mixer". At the THz frequency region, the resistive mixer can be applied for FETs with short gate case.

b. Long gate ($L \gg (\rho C\omega)^{-1/2}$)

The AC current is induced in the channel and leaks to the gate from the source side at a small distance l. The leakage length l has the value of $(\rho C\omega)^{-1/2}$. The leakage length is called "characteristic length", and its value is equal to $s(\tau/\omega)^{1/2}$. If $l \ll L$, both AC voltage and current cannot exist in the channel near the drain side of FET. In this case, the FET can act as a nonresonant detector for the plasma wave.

The FET can gather the electrons in the channel as a 2DEG, which acts as electron fluid in the channel of FET. The concentration of the electron in the channel depends on applying gate-to-channel voltage:

$$en = CU, \tag{1}$$

where e is the elementary charge, n is the electron concentration in the channel of FET, C is the gate-to-channel capacitance per unit area, and U is the gate-to-channel voltage. The AC voltage, which is induced by the THz radiation between the source and the gate, can modulate the electron concentration n, and thus a DC current will arise. The plasma wave can propagate as an electron fluid in the channel of FET.

The propagation of the plasma wave definitely depends on the electron mobility μ, which affects the electron momentum relaxation time $\tau = \mu m/e$, where m is the effective electron mass, and plasma wave velocity s. The velocity of plasma wave s is given by [27]

$$s^2 = s_0^2 \left[1 + \exp\left(-\frac{eU_0}{\eta k_B T}\right)\right] \ln\left[1 + \exp\left(\frac{eU_0}{\eta k_B T}\right)\right], \tag{2}$$

where $s_0 = (\eta k_B T/m)^{1/2}$, $\eta = 1+(C_{dm}/C_{ox})$ is the ideality factor as the fitting parameter which is closely connected with the subthreshold regime of the FET, C_{dm} is the depletion capacitance, C_{ox} is the oxide capacitance, $U_0 = V_g - V_{th}$ is the gate overdrive voltage, and V_{th} is the threshold voltage. When $U_0 < 0$ and $|U_0| > \eta k_B T/e$ (i.e., in subthreshold region), Eq. (2) yields $s^2 = s_0^2$. The propagation distance of the plasma wave l, which is the important parameter of the nonresonant THz detector, is calculated as $s(\tau/\omega)^{1/2}$. Since the frequency of plasma wave ω can distinguish two regimes of the operation of the THz detector, the parameter $\omega\tau$, which is called the resonance quality factor, is a key factor of the THz detection. The operation of the THz wave detector is settled by $\omega\tau$ and the gate length L_g. If $\omega\tau > 1$, the plasma wave is underdamped and the FET can operate as a resonant detector if the propagation distance l of the plasma wave is longer than L_g of FET. The plasma wave can arrive in the drain side of the FET, and be reflected. When $\omega\tau < 1$, the plasma wave cannot exist due to an overdamping and the FET operates in nonresonant regime.
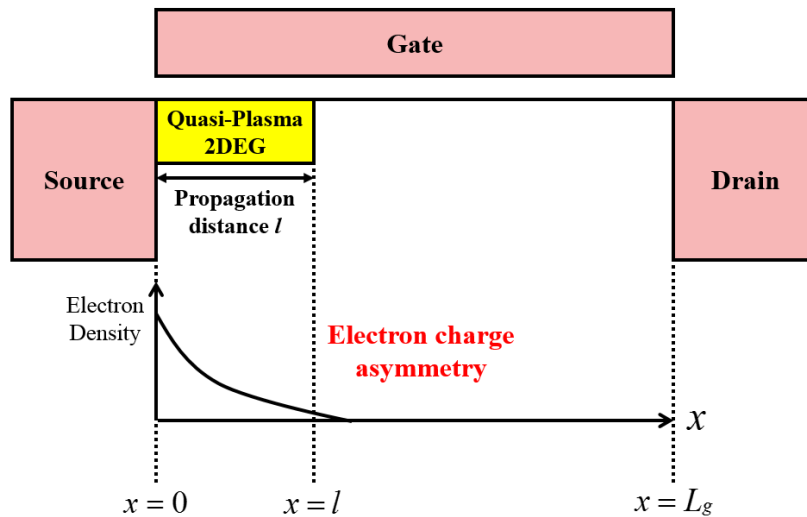
(a)
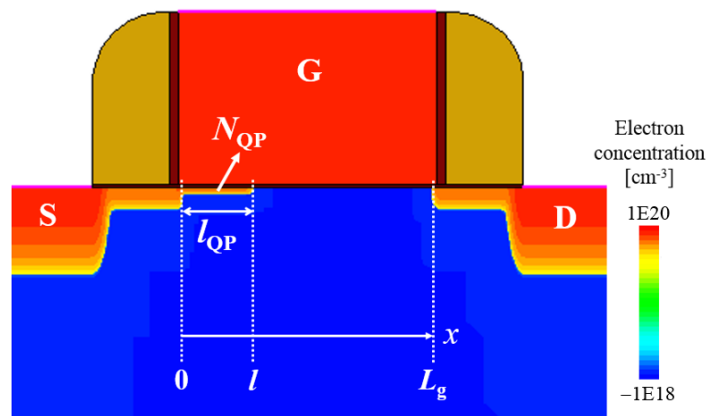
(b)

Figure 1-6. (a) Asymmetry of the plasma 2DEG distribution in the channel region of FET for THz detection in

nonresonant regime. (b) Structure of Si FET-based THz detector and TCAD simulation framework with quasi-plasma 2DEG modeling.

Figure 1-6(a) shows the description of the plasma 2DEG density distribution in the channel region of Si FET. When $L_g \gg l$, the plasma wave, which is excited at the source side of the channel, cannot reach the drain side because the plasma wave decays near the source side before reaching the drain side. In this case, the FET can operates as a nonresonant THz detector, and it is possible to analyze behaviors of the plasma wave by using continuity equation and hydrodynamic Euler equation [11, 12], which are given by

$$\frac{\partial n}{\partial t} + \frac{\partial (nv)}{\partial x} = 0 , \tag{3}$$

$$\frac{\partial v}{\partial t} + v \frac{\partial v}{\partial x} = -\frac{e}{m}\frac{\partial U}{\partial x} - \frac{v}{\tau} , \tag{4}$$

where v is the electron drift velocity, $\partial U/\partial x$ is the electric field along with the carrier transport direction in the channel, and v/τ is the external friction term which explains collisions between electrons and phonons (or impurities) [11, 12]. By combining linearized Eq. (3) with Eq. (4), the output detecting signal, which is actually a photoinduced drain-source voltage ΔU, is obtained as follows:

$$\Delta U = \frac{1}{4}\frac{U_a^2}{U_0}\left[1 + \frac{2\omega\tau}{\sqrt{1+(\omega\tau)^2}}\right] , \tag{5}$$

where U_a is the amplitude of incident THz EM wave. From Eq. (5), it is noticeable that the maximum of ΔU for the incident THz EM wave is achieved when $U_0 = 0$ (i.e., $\Delta U = \infty$) and then ΔU will gradually decrease as U_0 increases (i.e., $V_g > V_{th}$). When T > 0 K, however, U_0 never becomes zero even if V_g approaches V_{th} owing to the Fermi-Dirac distribution [28].

Figure 1-6(b) shows the structure of FET-based THz detector and circuit configuration with the AC voltage as the incoming THz source, which induces the photoresponse ΔU as the DC voltage difference between the source and drain side. By applying the quasi-plasma 2DEG model, it is possible to overcome the limitation of the TCAD simulation platform without hydrodynamic formalism, and thus, we demonstrate the THz detection in nonresonant regime.

In order that performance enhanced of plasmonic THz detector based on MOSFET behaviors is developed, it is required to set up the well-established MOSFET device simulation and modeling environment such as the technology computer-aided design (TCAD) platform, because TCAD

7

platform provides a versatile and reliable simulation framework based on the advanced MOSFET models for the exact analysis and the efficient structure design of the THz detector based on the MOSFETs. While the carrier transports of FET in transit mode such as drift and diffusion can be represented by using TCAD platform, however, there exists the limitation of TCAD that it cannot analyze the plasma wave dynamics as the electron fluid because the hydrodynamic formalism has not yet been included in TCAD platform [29, 30]. Hence it is essential to develop the innovative TCAD model for analysis of the THz detector based on FET.

1.2.3 Issues of Research on Terahertz Detector
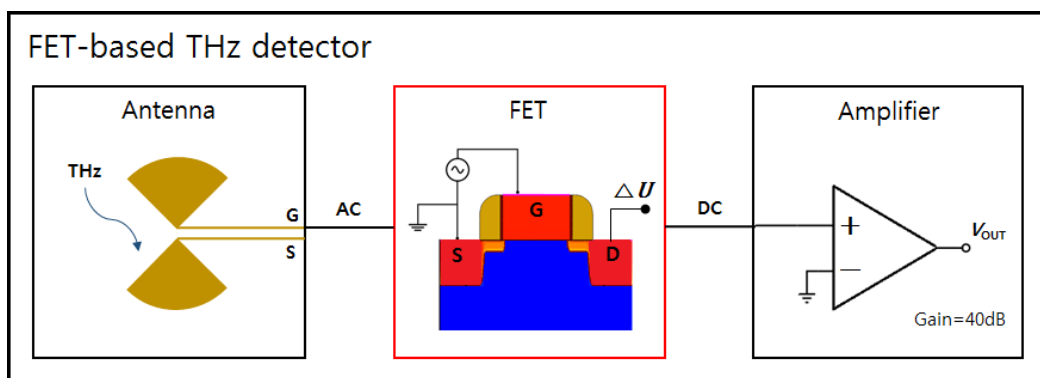
Figure 1-7. Conventional configuration of FET-based THz detector. There are three parts of the THz detector based on FET: antenna, FET, and amplifier

A. Component analysis of THz detector technology

Conventional FET-based THz detector is composed of three parts: antenna, FET, and amplifier. As an operation principle of FET-based THz detector, the THz wave radiation is transferred through the antenna to FET as an input AC voltage signal and the asymmetrically induced channel charge of FET produce the photoresponse (ΔU) as an output DC voltage, which can be amplified through the amplifier.

The most fundamental and significant issue in conventional FET-based THz detector is the very low-level photoresponse (ΔU) (i.e. low performance). This output ΔU level is still comparable with the background noise level, so lock-in amplifier (big hardware) and/or the DC voltage amplifier with very high-gain dynamic range should be incorporated in the output stage. Considering a feasible multi-pixel THz detector, however, these amplifiers cannot be integrated into each detector pixel of multi-pixel array.

B. Performance-limiting issues of THz detector technology

Before the specific technical issues related with performance limits are addressed, the performance metrics of FET-based THz detector should be carefully investigated. There are two typical

performance metrics: responsivity (R_V) and noise equivalent power (NEP), which can be expressed as follows.

$$R_V = \frac{\Delta U}{P_a}, \tag{6}$$

$$NEP = \frac{N}{R_V} = \frac{(4k_B T R_d)^{0.5}}{R_V}, \tag{7}$$

where P_a is AC power, N is thermal noise of detector, and R_d is the channel resistance.

From Eq. (6), the best R_V can be achieved by making the output ΔU level of FET as high as possible under the same input power from THz source. By definition of Eq. (7), the best NEP can be obtained by keeping total noise of detector as low as possible under the same R_V. The key factor for the highest R_V and the lowest NEP is the photoresponse ΔU in FET stage, which means that ΔU of FET (not R_V of detector) should be up to the breakthrough-level along with reducing the total noise of detector.

1.3 Motivation

Considering a feasible multi-pixel THz detector, however, these amplifiers cannot be integrated into each detector pixel of multi-pixel array. To remove this conventional output amplification stage, the output ΔU in FET stage should be enhanced up to the level of after-amplification, and thus, this is the reason why the performance-breakthrough technology research is essential in FET-based THz detector for multi-pixel and real-time THz imaging.

In the conventional approach based on configuration of figure 1-7, however, only R_v enhancement approach has been performed recently. Since the lack of research on the photoresponse ΔU in FET itself, it is necessary to mainly focus on the circuit design approach such as adding additional components (e.g. capacitors, FETs) and high-gain amplifier stage. There have been the following two technical limiting the detector performance. One thing is the increase of the total detector noise by these additional components, and the other is that device-level research on FET itself has not existed yet for multi-pixel THz array detector. Therefore, the THz detector performance-breakthrough research focus should be on a device-level FET stage (in figure 1-7) for a feasible multi-pixel real-time THz imaging application.
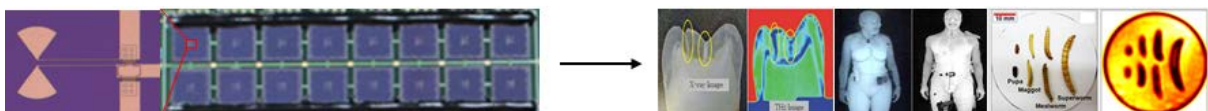
Figure 1-8. FET-based multi-pixel THz detector array and its imaging application

1.4 Thesis overview

In this thesis, I propose accurate analysis and modeling of the Si FET-based THz wave detector using both TCAD and SPICE simulation. Firstly, I reviewed the applications and the operation principles of the THz wave detector, and bring up a topic in the introduction. In section II, I present the modeling and simulation results for the physical analysis of the photoresponse enhancement according to the gate oxide scaling in nanoscale Si FETs with quasi-plasma 2DEG model. By using the new normalization method based on mobility change in the channel, the accurate analysis and characterization of the quasi-plasma 2DEG model are introduced. In section III, the new NQS compact model of MOSFET-based THz wave detector is proposed for the analysis of fast switching and high-frequency operation. For demonstration of the new NQS model as the THz wave detector, the transient simulation results with TCAD-based verification and photoresponse simulation results are presented. In section IV, I applied a summary and conclusions, and finally, the future works are presented in section V. This thesis is based on my papers in journal and conferences.

Chapter 2

Numerical Device Modeling of Terahertz Wave Detector Based on Si FET

2.1 Modeling of Terahertz Wave Detector with Quasi-Plasma 2DEG
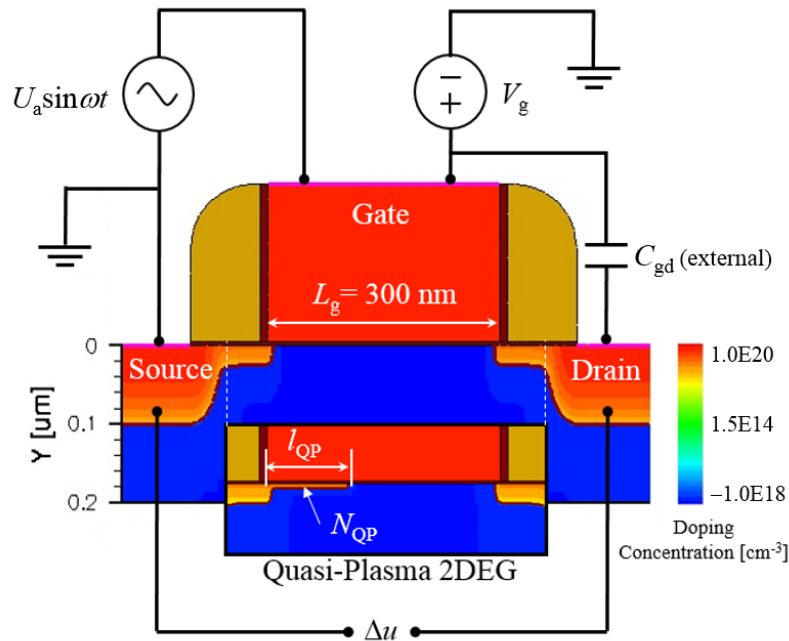
Figure 2-1. The structure of THz detector based on Si FET and TCAD simulation framework. The external capacitor C_{gd} is connected between the gate and drain side of FET for asymmetric boundary condition.

As shown in figure 2-1, n-type Si MOSFET structure has been designed by TCAD simulation with the several structure parameters such as the gate length $L_g = 300$ nm, the junction depth of the source and drain $X_j = 100$nm, the channel doping concentration $N_{ch} = 1\times10^{18}$ cm^{-3}, the source and drain doping concentration $N_d = 1\times10^{20}$ cm^{-3}, poly-Si gate doping concentration $N_{poly} = N_d$, and lightly doped drain (LDD) concentration $N_{LDD} = 1\times10^{19}$ cm^{-3}.

When the THz wave irradiates on the FET-based detector, the photoresponse is induced in the

channel by asymmetric boundary condition between the source and the drain. This DC voltage difference between the source and the drain is originated by the electron charge asymmetry as a 2DEG in the channel. The propagation length of the plasma wave, which is called the characteristic length, is considered an important parameter for electron charge asymmetry as 2DEG in the channel region. The key point for extracting the photoresponse is to characterize and analysis accurately the characteristic length as 2DEG length and 2DEG density in the channel. Since the structure design of FETs in frequency and time domain costs a great deal, the numerical solution of the continuity equation and hydrodynamic Euler equation with Poisson's equation is necessary for the accurate analysis of the plasma wave 2DEG behavior. In the nonresonant regime of THz detection ($\omega\tau < 1$), the overdamped plasma wave cannot exist in the drain side of the channel. This phenomenon leads to the asymmetry of the electron density distribution in the channel region of the FET. Therefore, we introduce the quasi-plasma electron box as a 2DEG [31], which is the overdamped plasma wave in the channel, for the asymmetric boundary condition and electron density distribution in the channel.

2.2 Asymmetric Boundary Condition of Terahertz Detector
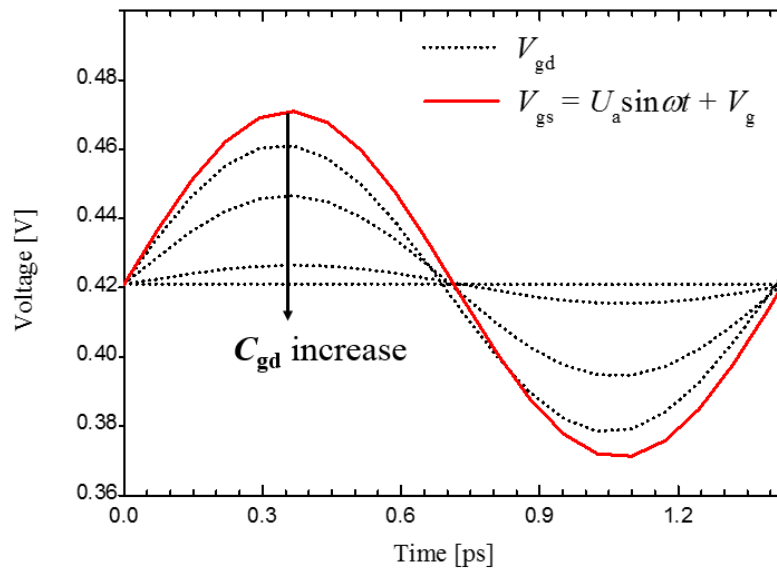
Figure 2-2. Transient simulation results of the FET-based THz detector using the TCAD platform with asymmetric boundary condition between the source and drain by integrating the external capacitor (C_{gd}).

The asymmetric condition should be needed for extracting ΔU of the THz detector based on Si FET in nonresonant regime. Figure 2-2 shows the transient simulation results of of the FET-based THz detector using the TCAD framework with the asymmetric condition between the source and drain by adding varied external capacitance between the gate and drain. The gate-to-source voltage V_{gs} has the

fixed value of $U_a\sin\omega t + V_g$, however, the gate-to-drain voltage V_{gd} has been saturated to DC output voltage as external gate-to-drain capacitance C_{gd} increases. Thus, we obtain the asymmetric boundary condition in our device by integrating the C_{gd} for THz detection.

Figure 2-3 shows propagation and modulation of the plasma wave as 2DEG at frequency $f = 0.7$ THz has been explained with TCAD transient simulation. The contour plots of the 2DEG density modulation (when $t_{ox} = 2.5$ nm) along with the channel at each time scale indicate the change of the 2DEG density modulation according to increasing C_{gd}.
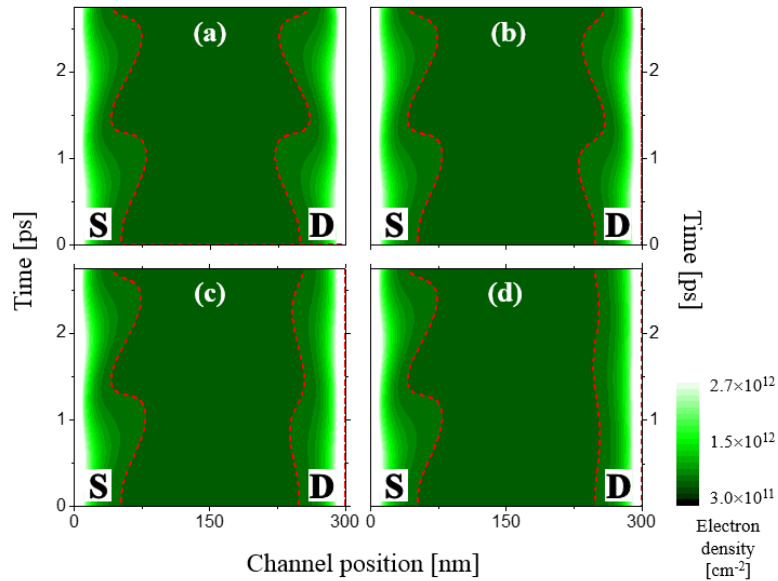
Figure 2-3. Contour plots of the electron density modulation along with the channel position at each time scale in 2 cycles. The channel 2DEG density is modulated by incoming THz radiation at $f = 0.7$ THz with (a) symmetric boundary condition (when $C_{gd} = 0$), (b) $C_{gd} = 1$ aF, (c) $C_{gd} = 1$ fF, and (d) $C_{gd} = 1$ pF.

For the symmetric boundary condition (in figure 2-3(a)), the plasma wave as 2DEG can propagate equally both at the source and drain side. By adding capacitance with the values of 1 aF, 1 fF, and 1 pF, as shown in Fig. 2-3(b), (c), and (d), respectively, the channel electron 2DEG propagates shorter than symmetric condition near the drain side. As the asymmetric boundary condition is almost completely satisfied at $C_{gd} = 1$ pF, the AC voltage has been applied only at the source side.
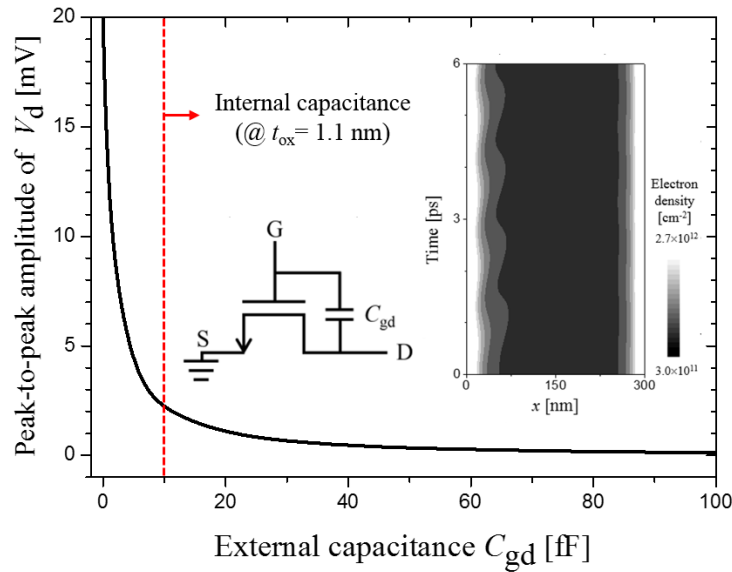
Figure 2-4. Simulation results of the peak-to-peak amplitude of the voltage difference between the gate and drain according to increasing gate-to-drain external capacitance (C_{gd}) at t_{ox}= 1.1 nm.

Figure 2-4 shows the transient simulation results of the TCAD framework at t_{ox} = 1.1 nm with adding the gate- to-drain external capacitance (C_{gd}), which is connected at the drain side only, because it is necessary to set up the asymmetric boundary condition between the source and drain side for extracting the photoresponse ΔU of the THz detector based on Si FET in nonresonant regime. The peak-to-peak amplitude of the voltage difference between the gate and drain (U_a) becomes almost zero in accordance with increase of C_{gd}. The asymmetric boundary condition by integrating C_{gd} is satisfied, if C_{gd} is larger than the internal capacitance of FET.

2.3 TCAD Simulation Results

The plasma wave behavior as 2DEG should be described by the hydrodynamic Euler equation with the convection component (= $v(\partial v/\partial x)$), however, the FET-based THz detector with the quasi-plasma 2DEG has been modeled by using the Synopsys[TM] *Sentaurus Device* TCAD framework, which does not include the hydrodynamic Euler equation. Even though the computational limit of the *Sentaurus* device TCAD platform, it is necessary to exploit the TCAD simulation for the simulation of the nonresonant THz detectors with quasi-plasma 2DEG owing to the well-established MOSFET models and the accurate analysis environment on TCAD framework.

2.3.1 DC Characteristics
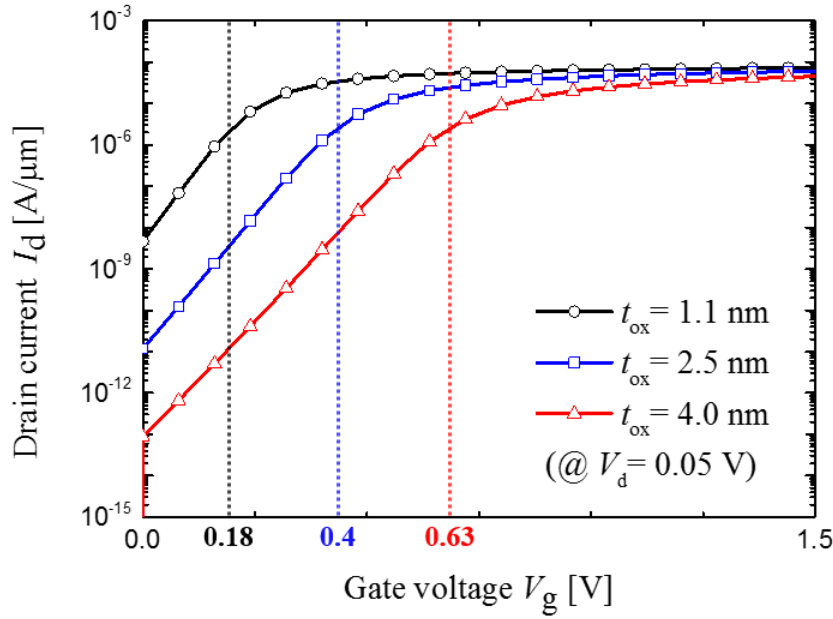
Figure 2-5. DC I_d-V_g characteristics of TCAD device simulation results. According to the variation of the gate oxide thickness (t_{ox} = 1.1, 2.5, and 4 nm), the threshold voltage V_{th} have been extracted at the linear region (V_d= 0.05 V).

Table I. DC characteristics (V_{th} and SSW) of the FET-based THz detector according to the t_{ox}.

t_{ox} [nm]	V_{th} [V]	SSW [mV/dec]
1.1	0.18	68.5
2.5	0.40	78.7
4.0	0.63	92.5

The simulation results of DC characteristics, such as the threshold voltage (V_{th}) and subthreshold swing (SSW) have been extracted by using the TCAD framework in order to investigate the effect of the t_{ox} scaling (in Table I). According to the increase of the gate oxide thickness (t_{ox} = 1.1, 2.5, and 4 nm), the threshold voltages of FETs, which have been extracted by transconductance (g_m) extrapolation method in linear region (at V_d= 0.05V) [32], also increase (V_{th}= 0.18, 0.4, and 0.63 V). In accordance with the gate voltage difference, the greater change of current will be acquired due to the enhanced normal field. Therefore, we can obtain the improved SSW of FET through the t_{ox} scaling.

2.3.2 Electron Mobility in Channel Region

The plasma wave behavior as the 2DEG of the THz detector can be represented as the electron density in the channel of FET. Because the plasma wave velocity s and the electron momentum relaxation time τ, which are important factor of the THz wave detector, definitely depend on the electron mobility, the modulation and propagation of the plasma wave is influenced by the electron

15

mobility. Therefore, the electron mobility should be extracted in nonresonant mode of the THz detection in order to analyze the electron density in the channel.

Figure 2-6 shows the simulation results of the electron mobility as a function of the channel position at each time t in a cycle T. Regardless of t_{ox}, the gate overdrive voltage swing U_0 should have the fixed value (at $U_0 = V_g - V_{th} = -0.1$ V), because the electron density is extremely sensitive by the biased gate voltage. The electron mobility at the source side is smaller than at the drain side due to the asymmetry of the channel 2DEG density distribution by adding the external capacitance between the gate and drain. For all THz detectors designed by TCAD framework, which take on the different values of the gate oxide thickness ($t_{ox} = 1.1$, 2.5, and 4 nm), minimum values of electron mobility near the source side is extracted at $t = (4/5)$T as shown in Fig. 2-6(a), (b), and (c).

The electron density at the source side in the channel is higher, the mobility is more degraded, because the electrons can be gathered more, and thus, the asymmetry of electron charge increases between the source and drain increases. Figure 2-7 shows the electron mobility degradation at the source side in the channel according to the decrease of t_{ox}. In accordance with scaling of t_{ox}, the electron mobility more decreases quantitatively as well as rapidly because of the surface roughness scattering (SRS), which is caused by the enhanced normal electric field from the gate, and thus, the channel 2DEG density increases owing to the better SSW.
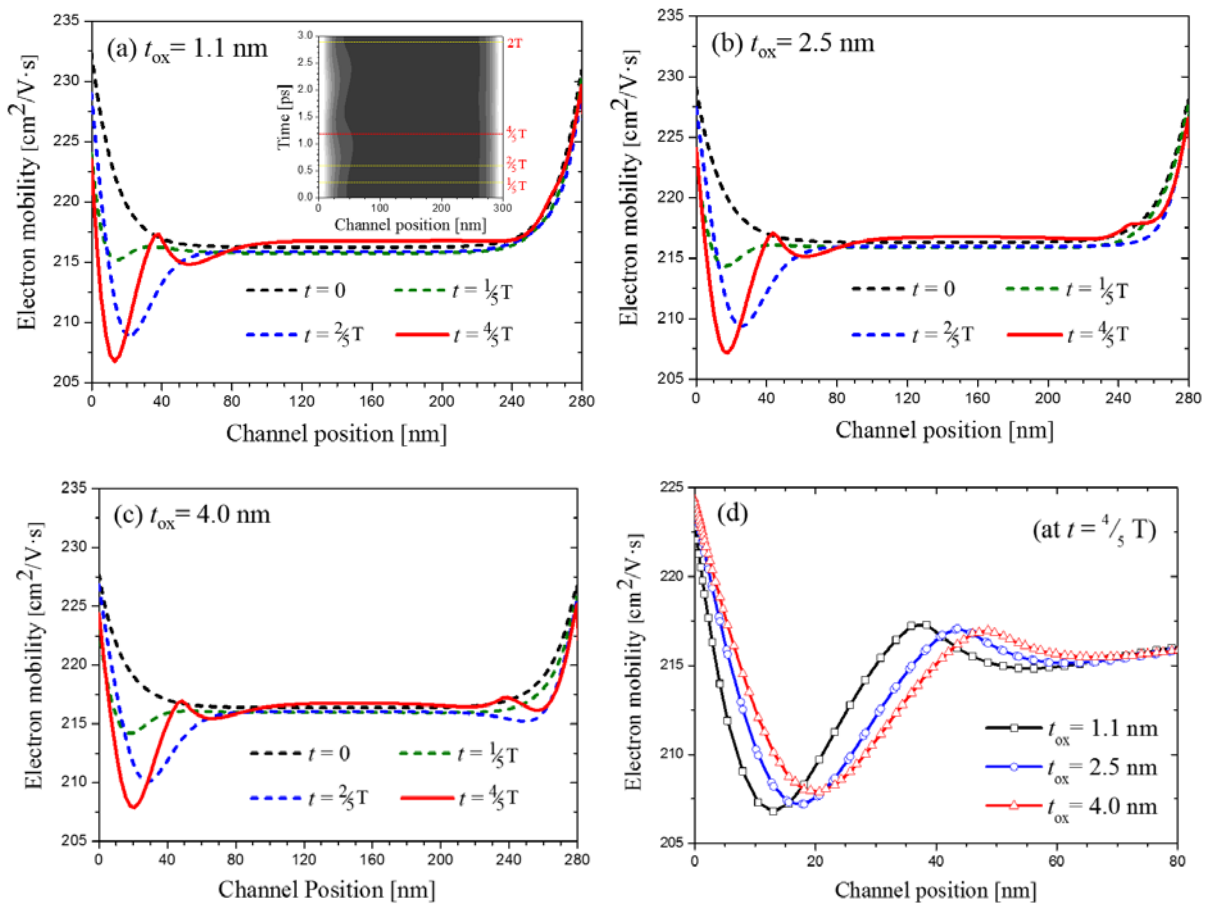
Figure 2-6. Simulation results of the electron mobility at each time scale along with the channel position when the same gate overdrive voltage U_0 ($U_0 = V_g - V_{th} = -0.1$ V) is applied. The electron mobility declines near the source side at (a) $t_{ox} = 1.1$ nm, (b) $t_{ox} = 2.5$ nm, and (c) $t_{ox} = 4$ nm. (d) The electron mobility at the source side according to various t_{ox} when the minimum values of the electron mobility have been extracted at $t = (4/5)$T.

2.3.3 Normalization of Electron Density (l_{QP} and N_{QP})

The quasi-plasma electron box modeling for extracting the photoresponse is performed under the room temperature with the structure of the MOSFET-based THz detector. Two important parameters for modeling of quasi-plasma 2DEG are length (l_{QP}) and density (N_{QP}). The quasi-plasma 2DEG length l_{QP} is equal to the propagation length of the plasma wave, which is called the characteristic length, and the quasi-plasma 2DEG density N_{QP} is defined average of the 2DEG modulation.

Figure 2-7 shows the transient simulation results of the electron density modulation as a function of the channel position at $t = (4/5)$T according to the variation of t_{ox}. As the t_{ox} decrease, the electron density near the source side decreases more sharply, while the average electron density in the channel region is higher as shown in Fig. 2-7(a). We demonstrate the accurate analysis for the plasma wave behavior by using our normalization method, which can define and characterize l_{QP} and N_{QP} exactly. Figure 2-7(b) shows the normalization of the electron density (D_e) and the channel position (x) from the simulation results of the electron density in the channel (in Fig. 2-7(a)). In order to extract l_{QP} and N_{QP}, we found the average point of the electron density (D_e) along with the channel position (x) near the source side, where the average point of the instantaneous rate of the electron density $\partial(D_e)/\partial x = -1$, because the standard mean value of 2DEG length and density is exteriorized at this point.

By using normalization of the electron density, the values of l_{QP} and N_{QP} are obtained according to t_{ox}. (see Table 2). As the oxide thickness ($t_{ox} = 1.1, 2.5,$ and 4 nm) increases, the quasi-plasma 2DEG length l_{QP} also increases while the quasi-plasma 2DEG density N_{QP} decreases owing to the difference of the electron mobility degradation near the source side.
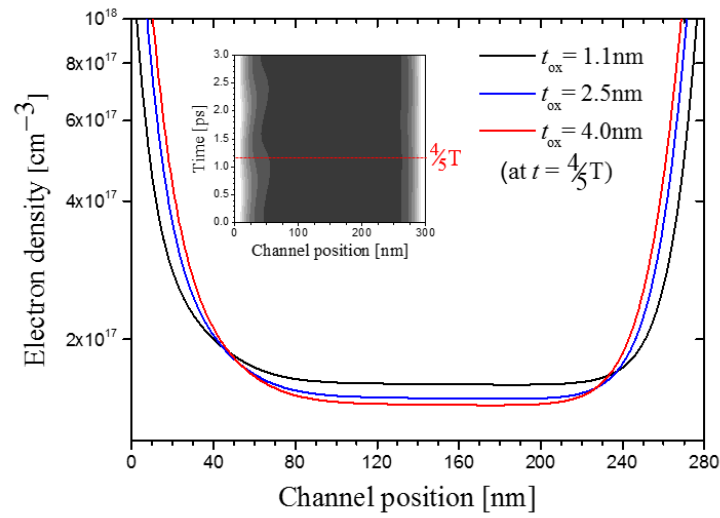
(a)
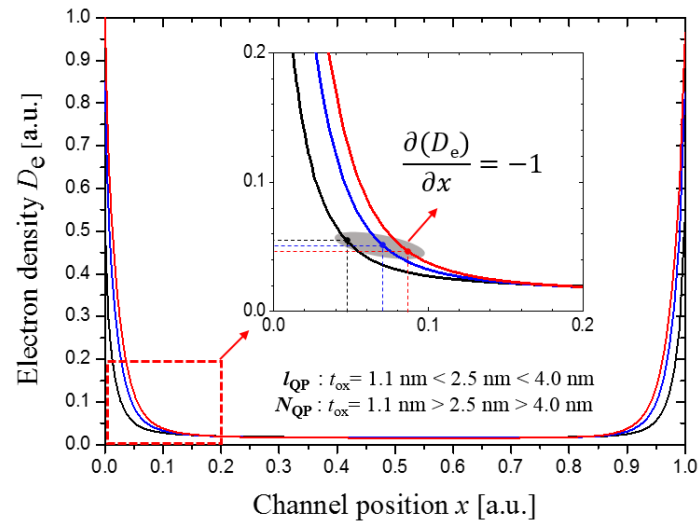
(b)

Figure 2-7. (a) Transient simulation results of the electron density D_e in the channel region x according to various t_{ox} at $t = 4T/5$ (= 1.2 ps) (b) Normalization of the electron density D_e along with the channel position x. Inset shows the average point of the electron density ($\partial(D_e)/\partial x = -1$) for extracting l_{QP} and N_{QP}.

Table II. The values of l_{QP} and N_{QP} from normalization of the electron density along the channel position according to the various t_{ox}.

t_{ox} [nm]	l_{QP} [nm]	N_{QP} [cm^{-2}]
1.1	12	5.3×10^{11}
2.5	20.6	5.25×10^{11}
4.0	25.7	5.2×10^{11}

In order to estimate these values of l_{QP} (in Table II), which have been obtained by the normalization of the channel electron density, it is essential to compare with analytic calculation results of

characteristic length l. In nonresonant regime with the low frequency ($\omega\tau < 1$), the l is given by $s(\tau/\omega)^{1/2}$. In the specific case ($U_0 < 0$ and $|U_0| > \eta k_B T/e$), if we consider $t_{ox} = 1.1$ nm, $\eta = 1.095$ so that $s = 1.64 \times 10^7$ cm/s. And thus, by using the extracted value of $\mu = 210$ cm^2/V-s from TCAD simulation results, τ is calculated to 0.02 ps. These values of analytical calculation finally yield $l = 11.5$ nm which is comparable to $l_{QP} = 12$ nm, which is extracted from quasi-plasma 2DEG model by using normalization method. Consequently, it is found that the quasi-plasma 2DEG length (l_{QP}) and propagation length of plasma wave (l) are actually same concept.

2.3.4 Performance of Terahertz Detector (Photoresponse and NEP)

By using the quasi-plasma 2DEG model with two structural key parameters of l_{QP} and N_{QP} into channel region, we obtain the simulation results of the two important performance metrics of the THz detector, such as responsivity R_v and noise equivalent power (NEP).

Figure 2-9 shows the simulation results of the Δu as a function of the V_g with various t_{ox}. Inset shows the simulation circuit configuration of the FET-based THz detector for extracting Δu. Under asymmetric boundary condition, Δu can be regarded as the offset voltage difference between the source and drain. The extracted values of Δu are normalized by the peak value in the subthreshold region ($V_g < V_{th}$) near $V_g = V_{th}$ with arbitrary unit. In the strong inversion region ($V_g > V_{th}$), Δu in the form of the DC voltage has a small value, because the voltage difference between the source and drain is almost zero as the channel is generated. According to the simplified theory of the THz wave detector in nonresonant regime, the peak values of Δu exist in the weak inversion region ($V_g < V_{th}$). As t_{ox} scaled down from 4 to 1.1 nm, the higher value of Δu has been obtained. In order to enhance the performance through the efficient structural device design such as scaling of t_{ox}, increment of the 2DEG density is the mainly factor for the high performance of THz detectors.

The responsivity R_v is given by $\Delta u/P_a$, where the AC power $P_a = 200$ nW, which is the comparable value from the experimental results [20]. Since the Δu significantly affects the responsivity, the graph of the responsivity with arbitrary unit has the almost same tendency. Figure 2-10 shows the calculation of the NEP from the R_v, which is the other performance of the THz detector. The NEP can be calculated as N/R_v (W/Hz$^{0.5}$), where $N = (4k_B T R_d)^{0.5}$ is the thermal noise of the FET-based THz detector. To estimate the thermal noise N, the channel resistance R_d is extracted from DC characteristics. The simulation results of Δu and NEP in the subthreshold region yield the theory of the nonresonant plasmonic THz detection. As t_{ox} is scaled down, minimum value of NEP is decrease by enhanced Δu [33].
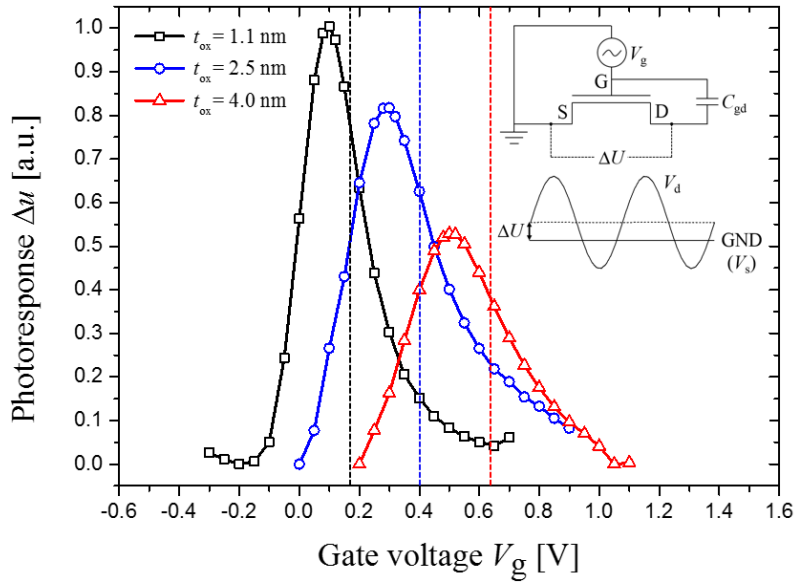
Figure 2-8. Simulation results of the photoresponse Δu as a function of gate voltage as the variation t_{ox} (= 1.1, 2.5, and 4 nm) with the quasi-plasma 2DEG in the channel. Dashed lines indicate the threshold voltage V_{th} (= 0.18, 0.4, and 0.63 V) with respect to t_{ox}. Inset shows the schematic circuit configuration for extracting the Δu.
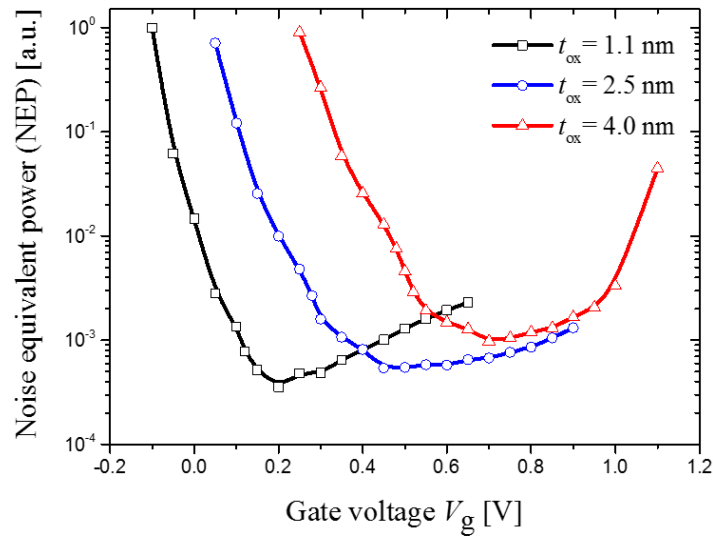
Figure 2-9. Calculation results of the noise equivalent power (NEP) by scaling of t_{ox}. The NEP can be calculated as N/R_v (W/Hz$^{0.5}$), where $N = (4k_B T R_d)^{0.5}$ is the thermal noise of the FET-based THz detector.

Chapter 3

New Non-Quasi-Static Compact Model for MOSFET-Based Terahertz Detector

3.1 Quasi-Static and Non-Quasi-Static Analysis

Not changed
by time

Changed by time
dramatically

| Static | Quasi-Static | Non-Quasi-Static | Dynamic |

Figure 3-1. Physical analysis according to the change of time.

Generally, there are four ways of the physical analysis according to the change of time: static, quasi-static, non-quasi-static, and dynamic analysis. Static analysis is the physical value analysis which is not changed by time, and dynamic analysis has the value variation which is changed by time dramatically. In MOS transistor modeling, quasi-static (QS) regime means that the charges can follow the change in voltage immediately without the time delay.

Because the MOSFETs have been widely used in commercial industries, it becomes necessary to estimate the circuit operation. Most of MOSFET models in SPICE operate in the QS regime, however, they have some disadvantages to predict the performance [34-37]. The signal changes slowly relative to the transit time of the device, so that the channel charge always is in steady-state region. When the rising time of input signal is longer than 20 times of the transit time of device, QS assumption is satisfied. In this condition, the transit time has different equation according to channel length in long channel case and short channel case. In the QS approximation, the carrier transit time along the channel region of FET is ignored, therefore, the QS approach may cause fatal error in simulation results for fast switching.

The non-quasi-static (NQS) analysis, which is applied to the variation of electron charge in the channel region of MOSFETs, is almost same topology in dynamic analysis. Because the design of MOSFET circuits demand the comprehension of NQS analysis for RF and transient simulation, many NQS MOSFET models have been established [38-52]. However, current NQS models are not available for SPICE circuit simulator.

At high frequency, the electron modulation in the channel is caused by incoming radiation, which induces the plasma wave in the source and drain side. In this situation, the analysis mode is related to oscillation period and transit time of plasma wave [7]. The plasma wave transit time is given by

$$\tau_t^{pl} = \sqrt{\frac{L^2 m}{e(V_g - V_{th})}} \tag{8}$$

where V_g is the gate voltage, V_{th} is the threshold voltage of the FET, and L is the channel length of the FET. In our MOSFET device, plasma wave transit time is about 10 ps. If the plasma wave transit time

through the channel is longer than the oscillation period of the incoming radiation, the NQS condition is fulfilled and the operating frequency region forms the THz gap. In this section, I propose the new NQS compact model for both transient and MOSFET-based plasmonic THz detector.
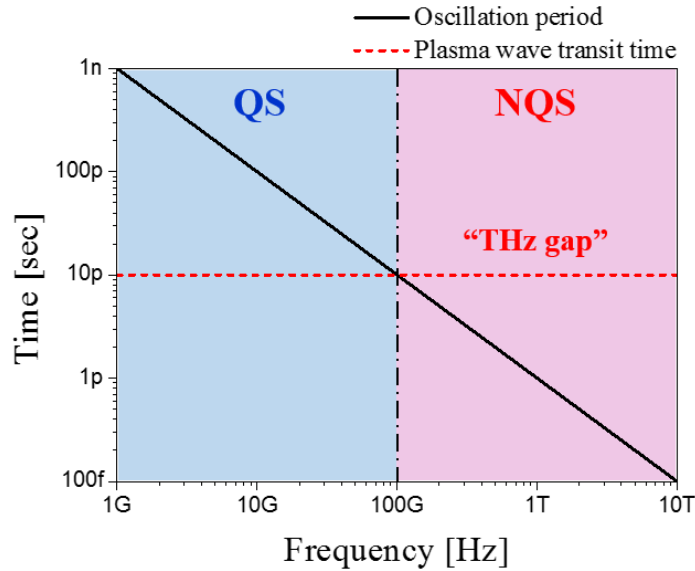
Figure 3-2. Oscillation period and transit time of the plasma wave according to the frequency. QS and NQS assumption have been distinguished when the oscillation period is equal to the plasma wave transit time.

3.2 DC Characteristics Matching between TCAD and SPICE

To build up the NQS compact model, I have treated two simulation tools, which are TCAD and SPICE. TCAD is a device-based simulation tool, and I can analyze the FET-based THz detector in NQS regime by using TCAD. For example, as shown in the figure 2-3, the simulation results of the electron density along the channel region can be extracted by using 2-D device simulation TCAD. On the other hand, SPICE is a circuit-based simulation tool. Especially, BSIM HSPICE is world widely used SPICE simulation tool, which is applicable for both QS and NQS analysis.

In order to demonstrate our new NQS SPICE model, I analyze the turn on switching transient simulation, which is the variation of the gate voltage and drain current according to the time. For accurate switching delay simulation and analysis, matching the simulation results of DC characteristic such as I_d-V_g curve between TCAD and SPICE tool is necessary [53].

Table III. Structure parameters of our TCAD device.

Parameter	Symbol	Value	Unit
Gate length	L_g	300	nm
Gate width	W	1	um

22

Substrate doping concentration	N_{sub}	1×10^{18}	cm^{-3}
Source and drain doping concentration	N_d	1×10^{20}	cm^{-3}
LDD doping concentration	N_{LDD}	1×10^{19}	cm^{-3}
Junction depth	x_j	0.1	um
Gate oxide thickness	t_{ox}	4	nm

Table IV. Input parameters for SPICE parameter extraction.

Name	Value	Unit	Description
L	300E-9	m	Gate length
W	1E-6	m	Gate width
TNOM	27	°C	Temperature
TOX	4E-9	m	Thickness of SiO$_2$
NCH	1E18	cm^{-3}	Channel doping concentration
NSUB	1E18	cm^{-3}	Substrate doping concentration
XJ	100E-9	cm^{-3}	Junction depth
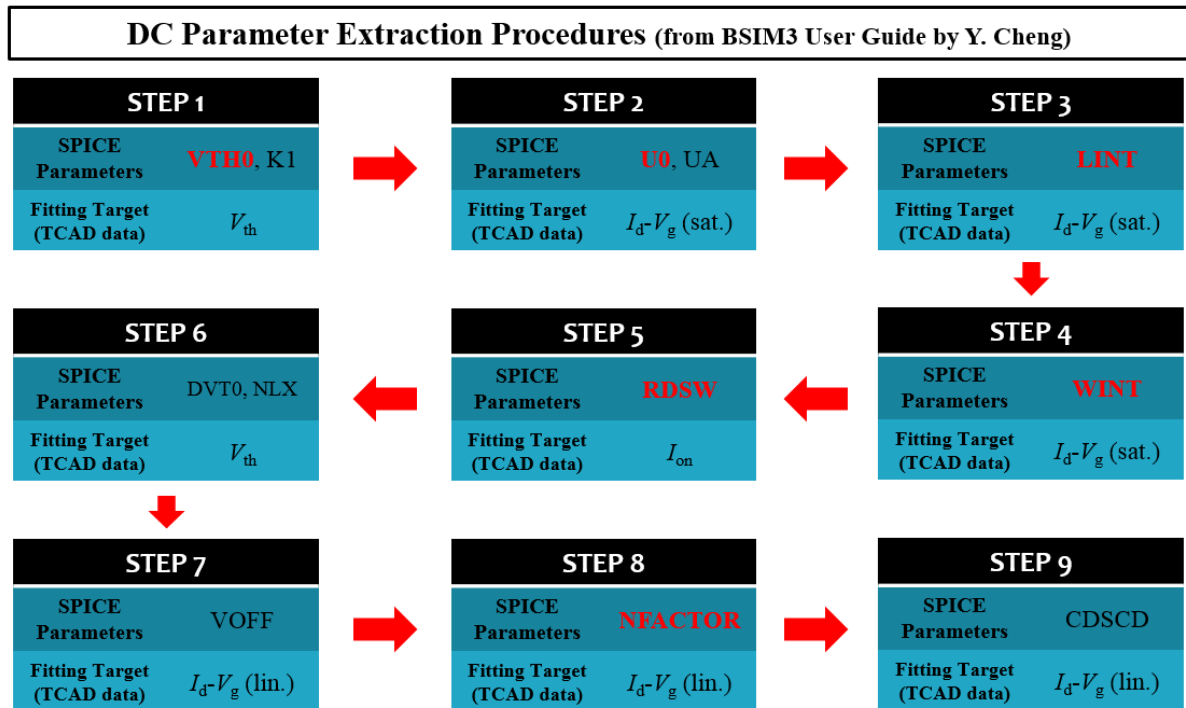
Figure 3-3. Main procedures of the DC parameter extraction in SPICE.

The parameters of the TCAD device structure is indicated in Table III. Using these parameters, I can get the basic parameters of SPICE and input parameters for SPICE DC parameter extraction (in Table IV). In SPICE, the parameters of lightly-doped drain (LDD) doping concentration have not existed, and unit of temperature is degree (not Kelvin) contrary to TCAD. Figure 3-3 shows the procedures of SPICE DC parameter extraction [54]. Originally, this procedure has twenty steps, however I simplify to nine important steps.

For efficient parameter extraction, the important parameters of SPICE for matching should be set to the proper value (in Table V). VTH0 is threshold voltage at $V_{bs} = 0$, U0 is the electron, LINT and WINT are structure fitting parameters, and RDSW and NFACTOR for subthreshold swing are critical parameters. Since all the other parameters are less important, they can be set to the default value. Figure 3-4 shows the DC simulation results of $I_d - V_g$ curve after parameter extraction procedures. The good matching between the TCAD and SPICE DC simulation is obtained. DC characteristics of SPICE simulation result both linear and saturation region are corresponded to TCAD simulation results.

Table V. Important SPICE parameter for DC matching between TCAD and SPICE.

Parameter	Description
VTH0	Threshold voltage when body voltage is zero.
U0	Electron mobility at T = TNOM
LINT	Length fitting parameter
WINT	Width fitting parameter
RDSW	Parasitic resistance
NFACTOR	SSW factor
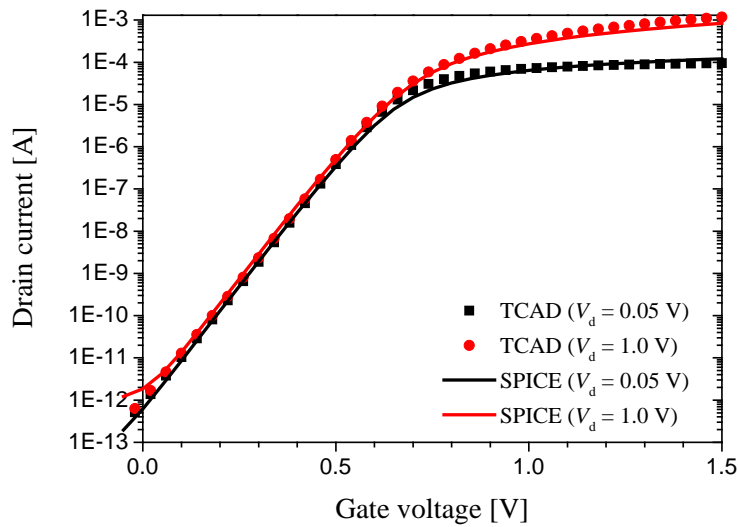
Figure 3-4. DC Id-Vg simulation results of MOSFET device after matching procedures. The good matching of DC characteristics between TCAD and SPICE has been obtained.

3.3 New Compact MOSFET Model for Non-Quasi-Static Analysis

As the MOSFET has been improved more performance-driven for THz detector, it is essential to estimate the circuit performance of FET in THz regime. However, most of the MOSFET models use the QS approach [34-37], where charging time of the carriers in the channel is ignored. Since the QS

assumption in MOSFET breaks down when the input signal changes on a time scale comparable to the transit time of FET, the NQS model of MOSFET is needed for the accurate analysis of fast switching and high-frequency operation.

3.3.1 Conventional NQS MOSFET Model
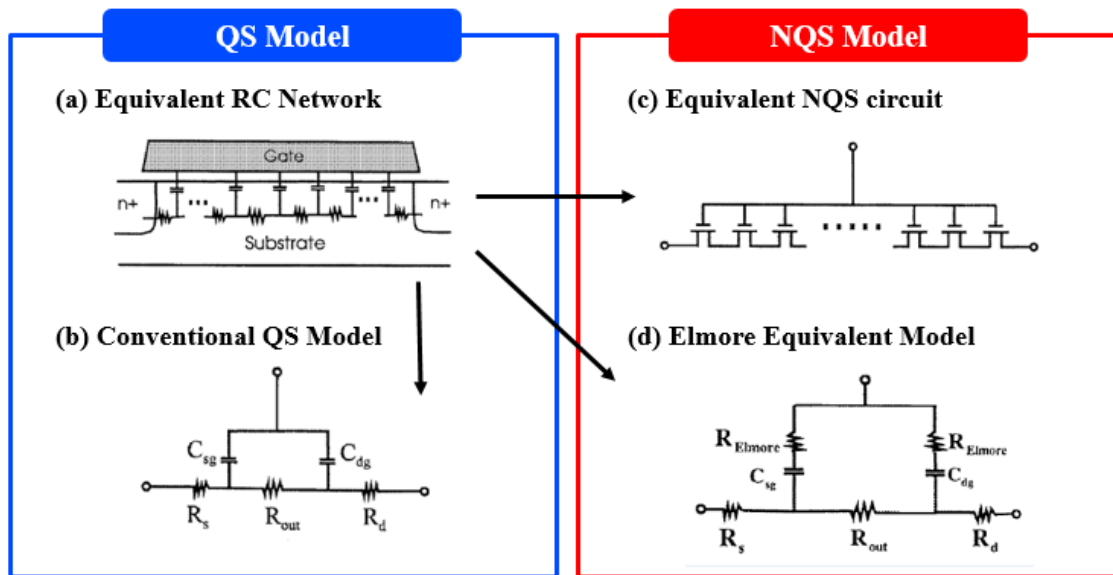
Figure 3-5. Several equivalent MOSFET model for time-varying analysis.

The channel of MOSFET can operate as a bias dependent RC distributed transmission line as shown in figure 3-5(a). Figure 3-5(b) shows the traditional circuit configuration of conventional MOSFET QS model. The gate and channel resistance are represented by lumped elements, and the gate capacitors are lumped to the source and drain nodes under the QS assumption. This model has been used in SPICE. For the QS approach, the delay time of channel charging is ignored. As shown in figure 3-5(c), the circuit equivalent through the transistors connected in series makes possible to analyze the NQS approximation [44]. In the NQS assumption, the delay time of the channel charge build-up can be estimated by incorporating the model equations. However, this circuit model requires a lot of calculation time and has the complexity of the formulation [43-48], so that new NQS compact model is needed for exact analysis of the channel charging delay. While these models work well for some applications, they fail to describe important small size device physics when operating at THz frequencies.

3.3.2 NQS Elmore model

Because the electron in the channel of FETs excited by THz frequencies, the channel contains plasma wave oscillations of electron density, which propagate along the channel. SPICE BSIM

simulation tool includes the NQS model, which is called by Elmore model [55, 56], therefore, we demonstrate the Elmore model in BSIM. Elmore model is one of the world-widely used NQS MOSFET model in SPICE, as shown in figure 3-5(d). Using NQS Elmore model, the RC distributed channel line can be approximated by the simple lumped circuit elements. Elmore model has the Elmore resistance (R_{Elmore}), which can be calculated from the channel resistance of MOSFET in strong inversion region. R_{Elmore} is given by [55]

$$R_{Elmore} = \frac{L_{eff}}{(ELM)\mu_{eff}W_{eff}Q_{ch}},$$

(9)

where L_{eff} is the effective gate length, μ_{eff} is the effective electron mobility in the channel, W_{eff} is the effective gate width, and Q_{ch}, which is the instantaneous channel inversion charge, is equal to the value of $C_{ox}(V_{gs} - V_{th})$. The important factor of R_{Elmore} is the Elmore constant ELM, which is SPICE NQS model parameter. The default value of ELM is set to 5, and R_{Elmore} has the value of 320 Ω in our device.

However, NQS Elmore model is not valid to transient simulation and fast switching mechanism of MOSFET. As show in figure 3-6, NQS Elmore model has unstable operation for fast switching when the rising time T_R is very small. Therefore, new NQS MOSFET compact model should be needed to describe the transient fast switching and high-frequency operation at THz region.

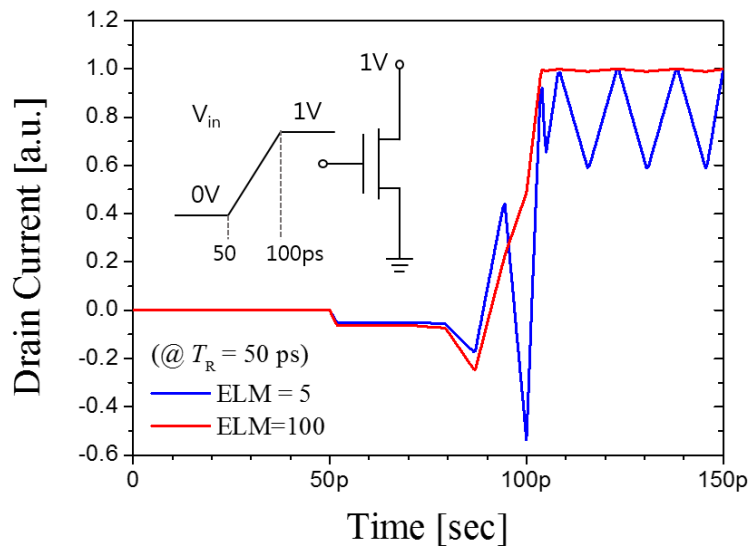Figure 3-6. Transient simulation result of NQS Elmore model in SPICE at T_R= 50 ps.

3.3.3 Transient Simulation of New Non-Quasi-Static MOSFET Model

To describe the switching delay in very short rising time, I have developed the new NQS compact

model of MOSFET. The implementation procedure of the new NQS MOSFET model based on SPICE circuit simulator. Figure 3-7 shows the circuit configuration of new NQS compact model of MOSFET with the lumped circuit elements R_g. This new model is applicable for transient simulation and works as the plasmonic THz detector.

In order to verify the new NQS MOSFET model of SPICE for transient simulation, the model has been compared with TCAD 2-D device simulation as reference of the complete numerical NQS simulation. For the comparison of SPICE and TCAD simulation, DC characteristics (I_d−V_g curve) matching between SPICE and TCAD has been achieved in section 3.2. Figure 3-8 shows the well-matched transient turn-on switching simulation results between the new NQS MOSFET model in SPICE and numerical TCAD simulation at $T_R = 40$ ps. This results indicate that our model is more accurate and reliable for fast switching mechanism than the existing NQS Elmore model.
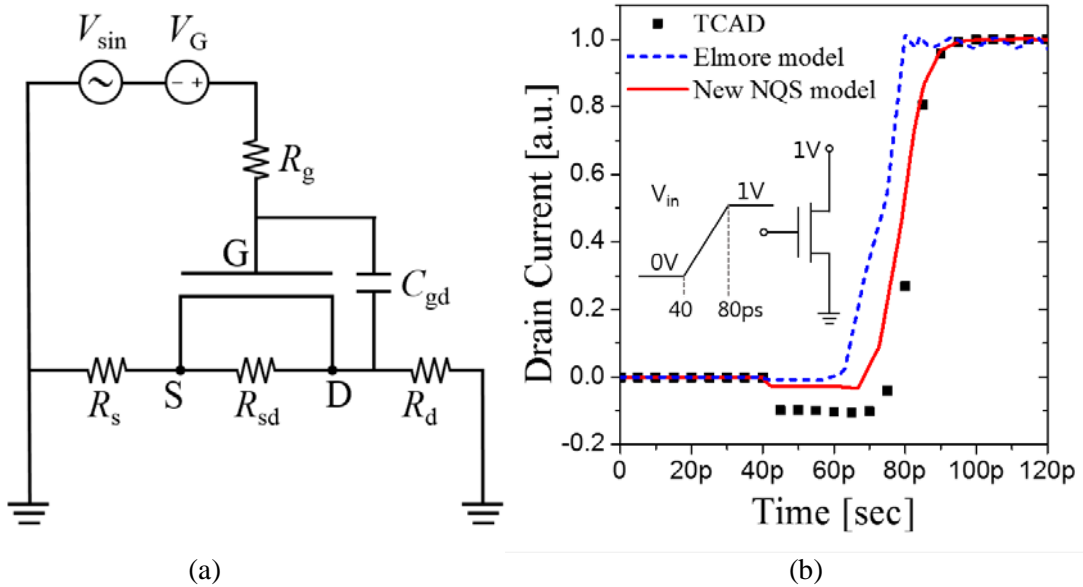
| (a) | (b) |

Figure 3-7. (a) Circuit configuration of new NQS compact model of MOSFET with the lumped circuit elements. (b) Transient simulation results of new NQS compact model of MOSFET with TCAD-based verification.

3.4 Demonstration of New NQS Compact Model for MOSFET-based THz Detector

The conventional MOSFET circuits have been modeled by using SPICE simulator. However, the compact models based on SPICE cannot represent the device physics of THz detector in the plasmonic mode, when the operation frequency are higher than the cut-off frequency. Using the new NQS compact MOSFET model, the MOSFET can act as a nonresonant detector at THz frequency region.
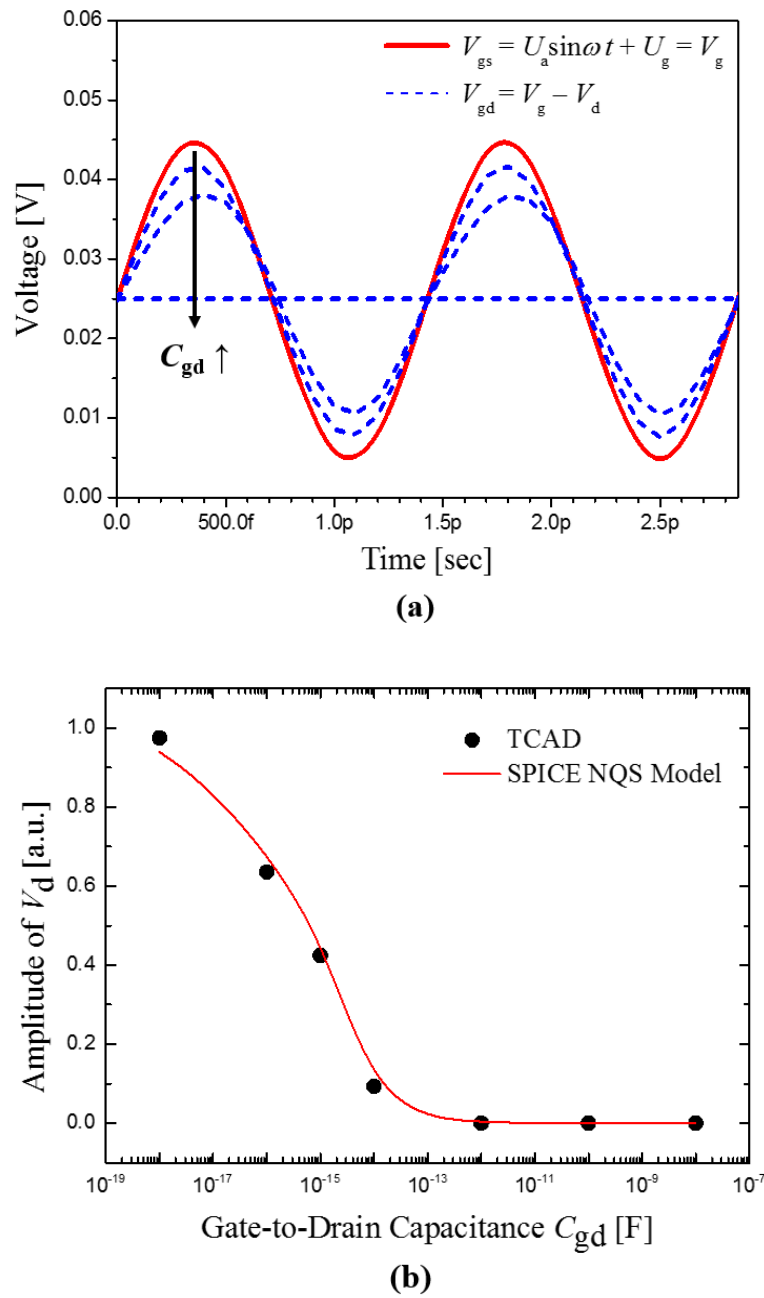
(a)

(b)

Figure 3-8. (a) The applied asymmetric boundary condition in simulation results of the new SPICE NQS MOSFET model by adding the various gate-to-drain capacitance C_{gd}. (b) Comparison of the drain voltage amplitude between TCAD and SPICE simulation results according to increase of C_{gd}.

In section II, I demonstrate the asymmetric boundary condition of the FET-based THz detector between the source and drain side by adding the gate-to-drain external capacitance on the basis of TCAD platform. The asymmetry of the nonresonant THz detector based on the new NQS MOSFET model has been implemented in the same way (by adding C_{gd}).

Figure 3-8(a) shows SPICE simulation results of the implemented asymmetric boundary condition between the source and drain side by adding varied external capacitance C_{gd} between the gate and

drain, because it becomes essential to obtain the photoresponse ΔU of nonresonant THz detector. The gate-to-source voltage (V_{gs}) has fixed value because the gate-to-source external capacitance is zero. On the other hand, the gate-to-drain voltage (V_{gd}) is saturated to DC output voltage according to the increase of C_{gd}. As shown in figure 3-8(b), simulation results of the new SPICE NQS MOSFET model are comparable to TCAD simulation results.

Finally, I demonstrate the validity of the new model by obtaining the successful photoresponse simulation as the function of the gate voltage at 0.2 THz. In order to extract the photoresponse, the new NQS MOSFET model has been set up as the voltage divider circuit between the channel resistance and load by adding the resistors R_s and R_d [57], as shown in figure 3-7. The peak point of the photoresponse is existed in the sub-threshold region in accordance with the simplified theory of the nonresonant THz detector [16]. The photoresponse has been simply extracted by using the new NQS compact model, so that the new NQS model can be exploited as the plasmonic THz wave detectors. The simulation results of the new NQS model in SPICE has the similar tendency of the measurement [20] and TCAD simulation results [33].
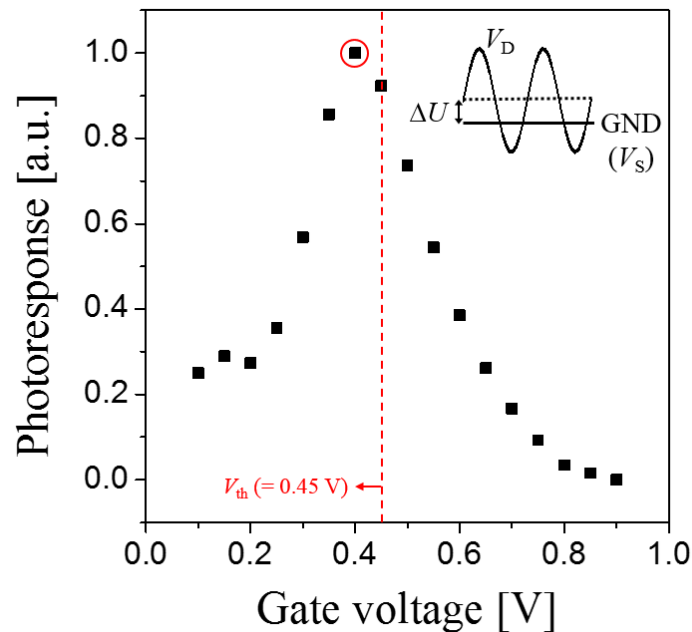
Figure 3-9. Simulation results of the photoresponse as a function of the gate voltage. In accordance with the simplified theory of the nonresonant THz detector, the maximum value of the photoresponse is located in the sub-threshold region (V_{th} = 0.45 V).

Chapter 4

Summary and Conclusions

In this thesis, I have reported that the quasi-plasma 2DEG model can provide the simulation framework for the advanced physical analysis of nanoscale Si FET-based plasmonic THz wave detector with efficient structural design in TCAD. By using our normalization method, two key parameters of the quasi-plasma 2DEG modeling, such as l_{QP} and N_{QP}, are exactly extracted. The reliable values of l_{QP} and N_{QP} can be obtained, and thus, I have demonstrated the performance enhancement of the THz detector based on FET according to scaling of t_{ox} with the quasi-plasma 2DEG model.

In addition, I have proposed the new NQS compact MOSFET model in SPICE simulation, which is applicable for both large-signal transient simulation and high-frequency operation. The model has been verified comparing with 2-D device simulation using TCAD which is the numerical NQS simulator. Finally, I demonstrate the validity of the new NQS model as the plasmonic THz detector through extracting the photoresponse, which is the performance of the THz detector.

Chapter 5

Future Works
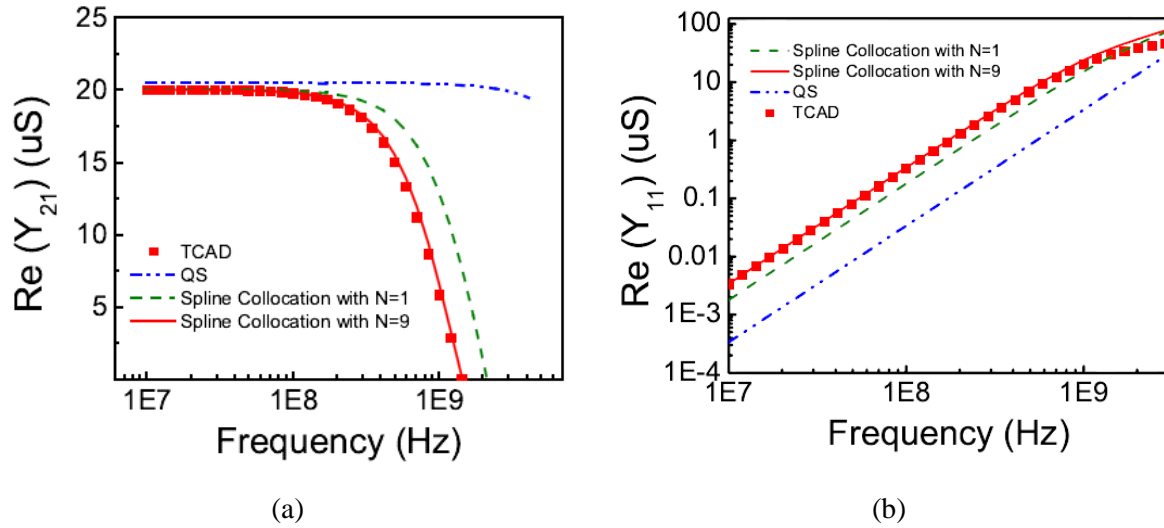
(a)　　　　　　　　　　　　　　　　　(b)

Figure 5-1. TCAD-based verification of RF simulation results. V_{gs} = 1.2 V, V_{ds} = 1.5 V [Ref. 53].

(a)　　　　　　　　　　　　　　　　　(b)
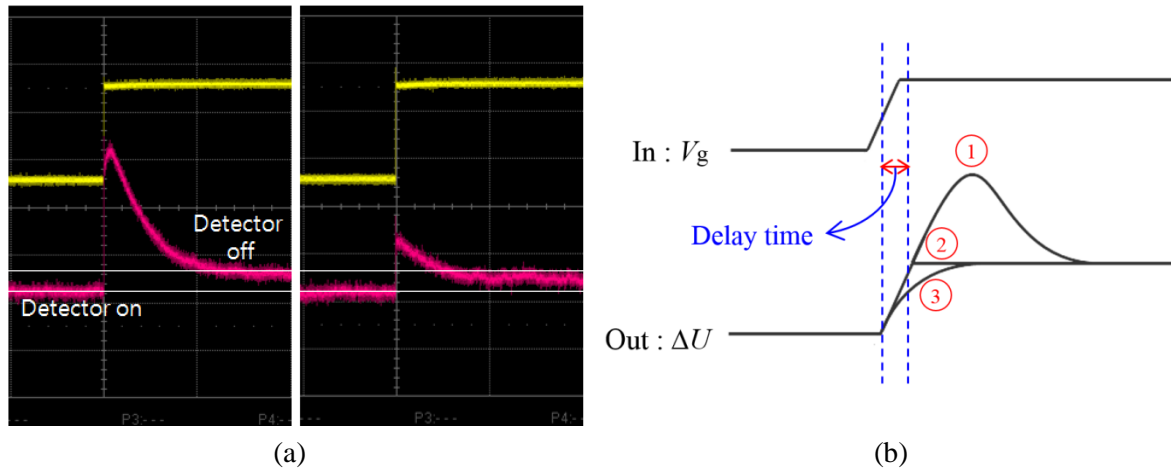
Figure 5-2. (a) Experimental results of the photoresponse when the input voltage is applied. (b) Block diagram of the input gate voltage and output photoresponse. By integrating the external gate capacitance, the parasitic capacitance will be eliminated and intrinsic delay time of the THz detector can be estimated.

　　In section III, I have proposed the new NQS compact model for MOSFET-based plasmonic THz wave detector. For validity of the NQS model, it becomes essential to verify the model for both transient and RF simulations. The new NQS model developed in section III should also be used to achieve the accurate RF MOSFET modeling, which is combined with the lumped circuit elements

(figure 3-7). The new NQS model for RF simulation will be verified using Y-parameter extraction. Comparison with the 2-D numerical simulation results (TCAD) will be implemented by a method similar to the transient simulation using the set of the SPICE model parameters, which accurately extract the transcapacitances and transconductances [53]. Figure 5-1 shows the previous work for the TCAD-based verification of RF simulation results, which demonstrate a good matching between analytical NQS MOSFET model and 2-D numerical simulation (TCAD).

In addition, the researches on delay of the plasmonic THz detector should be implemented for the performance enhancement of the plasmonic THz detector and real time THz imaging technology. As shown in figure 5-2(a), the experimental photoresponse results of the THz detection have the overshoot delay according to the input pulse signal. In this measurement, the overshoot delay of the photoresponse decreases by adding the external gate capacitance. On the SPICE simulation of MOSFET-based THz detector, the parasitic capacitance will be eliminated by integrating the external gate capacitance, so that overshoot delay of the photoresponse will be decrease and intrinsic delay time can be obtained. As a results, the delay of the THz detector for real time THz imaging will be demonstrated through the estimation of delay.

REFERENCES

1. P. H. Siegel, "Terahertz technology," *IEEE Trans. Microw. Theory Techn.*, vol. 50, no. 3, pp. 910–928, Mar. 2002.

2. B. Ferguson, S. Wang, D. Gray, D. Abbot, and X.-C. Zhang, "T-ray computed tomography," Opt. Lett., vol. 27, no. 15, pp. 1312–1314, Aug. 2002.

3. *Terahertz Sensing Technology, Volume I. Electronic Devices & Advanced Technology*, D. Woolard, W. Loerop, and M. S. Shur, Eds.. Singapore: World Scientific, 2003.

4. A. G. Markelz, "Terahertz dielectric sensitivity to biomolecular structure and function," *IEEE J. Sel. Topics Quantum Electron.*, vol. 14, no. 1, pp. 180–190, Jan./Feb. 2008.

5. Y. Ueno, R. Rungsawang, I. Tomita, and K. Ajito, "Terahertz images of biological molecules: frequency dependence of spatial resolution using a tunable terahertz laser source," *Jpn. J. Appl. Phys.*, vol. 47, no. 2S, pp. 1315–1320, Feb. 2008.

6. E. Ojefors, U. R. Pfeiffer, A. Lisauskas, and H. G. Roskos, "A 0.65 THz focal-plane array in a quarter-micron CMOS process technology," *IEEE J. Solid-State Circuits*, vol. 44, no. 7, pp. 1968–1976, Jul. 2009.

7. A. Lisauskas, U. Pfeiffer, E. Ojefors, P. H. Bolivar, D. Glaab, and H. G. Roskos, "Rational design   of high-responsivity detectors of terahertz radiation based on distributed self-mixing in silicon field-effect transistors," *J. Appl. Phys.*, vol. 105, pp. 114511-1–114511-7, 2009.

8. F. Schuster, D. Coquillat, H. Videlier, M. Sakowicz, F. Teppe, L. Dussopt, B. Giffard, T. Skotnicki, and W. Knap, "Broadband terahertz imaging with highly sensitive silicon CMOS detectors," *Opt. Exp.*, vol. 19, no. 8, pp. 7827–7832, Apr. 2011.

9. R. Han *et al*., "Active terahertz imaging using schottky diodes in CMOS: Array and 860-GHz pixel," *IEEE J. Solid-State Circuits*, vol. 48, no. 10, pp. 2296–2308, Oct. 2013.

10. Y. Zhao, E. Ojefors, K. Aufinger, T. F. Meister, and U. R. Pfeiffer, "A 160-GHz subharmonic transmitter and receiver chipset in an SiGe HBT technology," *IEEE Trans. Microw. Theory Techn.*, vol. 60, no. 10, pp. 3286–3299, Oct. 2012.

11. M. Dyakonov and M. Shur, "Shallow water analogy for a ballistic field effect transistor: New mechanism of plasma wave generation by dc current," *Phys. Rev. Lett*., vol. 71, no. 15, pp.

2465−2468, Oct. 1993.

12. M. I. Dyakonov and M. S. Shur, "Plasma wave electronics: Novel terahertz devices using two dimensional electron fluid," *IEEE Trans. Electron Devices*, vol. 43, no. 10, pp. 1640–1645, Oct. 1996.

13. V. Ryzhill and M. S. Shur, "Plasma wave electronics devices," in *Proc. ISDRS*, 2003, p. 200.

14. T. Nishimura, N. Magome, I. Khmyrova, T. Suemitsu, W. Knap, and T. Otsuji, "Analysis of Fringing Effect on Resonant Plasma Frequency in Plasma Wave Devices," *Jpn. J. Appl. Phys.*, vol. 48, no. 4S, pp. 04C096-1−04C096-4, Apr. 2009.

15. T. Nishimura, N. Magome, and T. Otsuji, "An Intensity Modulator for Terahertz Electromagnetic Waves Utilizing Two-Dimensional Plasmon Resonance in a Dual-Grating-Gate High-Electron-Mobility Transistor," *Jpn. J. Appl. Phys.*, vol. 49, no. 5R, pp. 054301-1−054301-7, May. 2010.

16. W. Knap, M. Dyakonov, D. Coquillat, F. Teppe, N. Dyakonova, J. Lusakowski, K. Karpierz, M. Sakowicz, G. Valusis, D. Seliuta, I. Kasalynas, A. El Fatimy, Y. M. Meziani, and T. Otsuji, "Field Effect Transistors for Terahertz Detection: Physics and First Imaging Applications," *J. Infrared Millim. THz Waves*, vol. 30, no. 12, pp. 1319−1337, Aug. 2009.

17. Y. Deng and M. S. Shur, "Electron mobility and terahertz detection using silicon MOSFETs," *Solid-State Electron.*, vol. 47, no. 9, pp. 1559−1563, Sep. 2003.

18. W. Knap, F. Teppe, Y. Meziani, N. Dyakonova, and J. Lusakowski, "Terahertz emission by plasma waves in 60 nm gate high electron mobility transistors," *Appl. Phys. Lett.*, vol. 84, no. 13, pp. 2331−2333, Mar. 2004.

19. N. Pala, F. Teppe, D. Veksler, Y. Deng, M. S. Shur, and R. Gaska, "Nonresonant detection of terahertz radiation by silicon-on-insulator MOSFETs," *Electron. Lett.*, vol. 41, no. 7, pp. 447−449, Mar. 2005.

20. R. Tauk, F. Teppe, S. Boubanga, D. Coquillat, W. Knap, Y. M. Meziani, C. Gallon, F. Boeuf, T. Skotnicki, C. Fenouillet-Beranger, D. K. Maude, S. Rumyantsev, and M. S. Shur, "Plasma wave detection of terahertz radiation by silicon field effects transistors: Responsivity and noise equivalent power," *Appl. Phys. Lett.*, vol. 89, 2006, Art. ID 253511.

21. W. Stillman, D. Veksler, T. A. Elkhatib, K. Salama, F. Guarin, and M. S. Shur, "Sub-terahertz testing of silicon MOSFET," *Electron. Lett.*, vol. 44, no. 22, pp. 1325-1327, Oct. 2008.

22. W. Knap, Y. Deng, S. Rumyantsev, J.-Q. Lu, M. S. Shur, C. A. Saylor, and L. C. Brunel, "Resonant detection of subterahertz radiation by plasma waves in a submicron field-effect transistor," *Appl. Phys. Lett.*, vol. 80, no. 18, pp. 3433–3435, May 2002.

23. W. Knap, V. Kachorovskii, Y. Deng, S. Rumyantsev, J.-Q. Lu, and R. Gaska, M. S. Shur, G. Simin, X. Hu, M. Asif Khan, C. A. Saylor, and L. C. Brunel, "Nonresonant detection of terahertz radiation in field effect transistor," *J. Appl. Phys.*, vol. 91, no, 11, pp. 9346–9353, June 2002.

24. A. El Fatimy, F. Teppe, N. Dyakonova, W. Knap, D. Seliuta, G. Valusis, A. Shchepetov, Y. Roelens, S. Bollaert, A. Cappy, and S. Rumyantsev, "Resonant and voltage-tunable terahertz detection in InGaAs/InP nanometer transistor," *Appl. Phys. Lett.*, vol. 89, 2006, Art. ID 131926.

25. W. Knap, F. Teppe, N. Dyakonova, D. Coquillat, and J. Lusakowski, "Plasma wave oscillations in nanometer field effect transistors for terahertz detection and emission," *J. Physics: Condensed Matter*, vol. 20, no. 38, p. 384205, 2008.

26. M. W. Ryu, J. S. Lee, K. Park, W-K. P, S-T. H, and K. R. Kim, "Photoresponse enhancement of plasmonic terahertz wave detector based on asymmetric silicon MOSFETs with antenna integration," *Jpn. J. Appl. Phys.*, vol. 53, no. 4S, pp. 04EJ05-1–04EJ05-4, Feb. 2014.

27. W. Knap, F. Teppe, Y. Meziani, N. Dyakonova, J. Lusakowski, F. Boeuf, T. Skotnicki, D. Maude, S. Rumyantsev, and M. S. Shur, "Plasma wave detection of sub-terahertz and terahertz radiation by silicon field-effect transistors," *Appl. Phys. Lett.*, vol. 85, no. 4, pp. 675–677, 2004.

28. V. V. Popov, D. V. Fateev, T. Otsuji, Y. M. Meziani, D. Coquillat, and W. Knap, "Plasmonic terahertz detection by a double-grating-gate field-effect transistor structure with an asymmetric unit cell," *Appl. Phys. Lett.*, vol. 99, 2011, Art. ID 233504.

29. J. N. Burghartz, *Guide to State-of-the-Art Electron Device*. Wiley-IEEE Press, Mar. 2013.

30. Sentaurus Device 3-D User Guide, *Synopsys*, Inc., March 2013.

31. H. C. Hwang, K. Park, W-K. Park, S-T. Han, and K. R. Kim, "Design and characterization of plasmonic terahertz wave detectors based on silicon field-effect transistors," *Jpn. J. Appl. Phys.*, vol. 51, no. 6S, pp. 06FE17-1–06FE17-7, June 2012.

32. A. Ortiz-Conde, F. J. Garcia Sanchez, J. J. Liou, A. Cerdeira, M. Estrada, and Y. Yue, "A review of recent MOSFET threshold voltage extraction methods," *Microelectron. Reliab.*, vol. 42, pp. 583–596, 2002.

33. M. W. Ryu, J. S. Lee, and K. R. Kim, "Physical modeling and analysis for performance enhancement of nanoscale silicon field-effect transistor-based plasmonic terahertz detector," in *Proc. 14th IEEE NANO*, Aug. 2014, pp. 971–974.

34. S. Y. Oh, D. E. Ward, and R. W. Dutton, "Transient analysis of MOS transistors," *IEEE J. Solid-State Circuits*, vol. SC-15, no. 4, pp. 636–643, 1980.

35. J. J. Paulous and D. A. Antoniadis, "Limitations of quasistatic capacitance models for the MOS transistors," *IEEE Electron Device Lett.*, vol. 4, pp. 221–224, 1983.

36. Y. P. Tsividis and G. Masetti, "Problems in the precision modeling of the MOS transistor for analog applications," *IEEE Trans. Computer-Aided Des.*, vol. 3, pp. 72–79, Jan. 1984.

37. Y. P. Tsividis and K. Suyama, "MOSFET modeling for analog circuit CAD: problems and prospects," *IEEE J. Solid-State Circuits*, vol. 29, no. 3, pp. 210–216, Mar. 1994.

38. C. Turchetti, P. Mancini, and G.Masetti, "A CAD-oriented non-quasistatic approach for the transient analysis of MOS ICs," *IEEE J. Solid-State Circuits*, vol. 21, no. 5, pp. 827-836, Oct. 1986.

39. H. J. Park, P. K. Ko, and C. Hu, "A non-quasi-static MOSFET model for SPICE—Transient analysis," *IEEE Trans. Electron Devices*, vol. 36, no. 3, pp. 561–576, Mar. 1989.

40. K.W. Chai and J. J. Paulos, "Unified nonquasi-static modeling of the longchannel four-terminal MOSFET for large- and small-signal analysis in all operating regimes," *IEEE Trans. Electron Devices*, vol. 36, no. 11, pp. 2513–2520, Nov. 1989.

41. E. Dubois and E. Robilliart, "Efficient non-quasi-static MOSFET's model for circuit simulation," in *IEDM Tech. Dig.*, 1995, pp. 945–948.

42. W. Liu, C. Bowen, and M.-C. Chang, "A CAD-compatible non-quasistatic MOSFET model," in *IEDM Tech. Dig.*, 1996, pp. 151–154.

43. S. W. Hwang, T.-W. Yoon, D. H. Kwon, and K. H. Kim, "A physics-based, SPICE (Simulation Program with Integrated Circuit Emphasis) —compatible non-quasi-static MOS (metal-oxide-semiconductor) transient model based on the collocation method," *Jpn. J. Appl. Phys.*, vol. 37, no. 2A, pp. L119–L121, Feb. 1998.

44. M. Chan, K. Y. Hui, C. Hu, and P. K. Ko, "A robust and physical BSIM3 non-quasi-static

transient and AC small-signal model for circuit simulation," *IEEE Trans. Electron Devices*, vol. 45, no. 4, pp. 834–841, Apr. 1998.

45. A. J. Scholten, L. F. Tiemeijer, P.W. H. de Vreede, and D. B.M. Klaassen, "A large signal non-quasi-static MOS model for RF circuit simulation," in *IEDM Tech. Dig.*, 1999, pp. 163–166.

46. J.-M. Sallese and A.-S. Porret, "A novel approach to charge-based nonquasi-static model of the MOS transistor valid in all modes of operation," *Solid State Electron.*, vol. 44, no. 6, pp. 887–894, Jun. 2000.

47. A.-S. Porret, J.-M. Sallese, and C. C. Enz, "A compact-non-quasi-static extension of a charge-based MOS model," *IEEE Trans. Electron Devices*, vol. 48, no. 8, pp. 1647–1654, Aug. 2001.

48. H. Wang, T.-L. Chen, and G. Gildenblat, "Quasi-static and nonquasistatic compact MOSFET models based on symmetric linearization of the bulk and inversion charges," *IEEE Trans. Electron Devices*, vol. 50, no. 11, pp. 2262–2272, Nov. 2003.

49. A. S. Roy, J. M. Vasi, and M. B. Patil, "A new approach to model nonquasi-static (NQS) effects for MOSFETs—Part I: Large-signal analysis," *IEEE Trans. Electron Devices*, vol. 50, no. 12, pp. 2393–2400, Dec. 2003.

50. A. S. Roy, J. M. Vasi, and M. B. Patil, "A new approach to model nonquasi-static (NQS) effects for MOSFETs—Part II: Small-signal analysis," *IEEE Trans. Electron Devices*, vol. 50, no. 12, pp. 2401–2407, Dec. 2003.

51. N. Nakayama, D. Navarro, M. Tanaka, H. Ueno, M. Miura-Mattausch, H. J. Mattausch, T. Ohguro, S. Kumashiro, M. Taguchi, T. Kage, and S. Miyamoto, "Non-quasi-static model for MOSFET based on carrier transit delay," *Electron. Lett.*, vol. 40, no. 4, pp. 276–278, Feb. 2004.

52. W.-K. Shih, S. Mudanai, R. Rios, P. Packan, D. Becher, R. Basco, C. Hung, and U. Jalan, "Predictive compact modeling of NQS effects and thermal noise in 90 nm mixed signal/RF CMOS technology," in *IEDM Tech. Dig.*, 2004, pp. 747–750.

53. H. Wang, X. Li, W. Wu, G. Gildenblat, R. van Langevelde, G. D. J. Smitt, A. J. Scholten, and D. B. M. Klaassen, "Unified non-quasi-static MOSFET model for large-signal and small-signal simulations," in *Proc. IEEE Custom Integr. Circuit Conf.*, Sep. 2005, pp. 823–826.

54. Y. Cheng and C. Hu, *MOSFET Modeling & BSIM3 Users Guide*.　Norwell, MA: Kluwer, 1999.

55. W. C. Elmore, "The transient response of damped linear networks with particular regard to wideband amplifiers," *J. Appl. Phys.*, vol. 19, no. 1, pp. 55–63, 1948.

56. L. T. Pillage and R. A. Rohrer, "Asymptotic waveform evaluation for timing analysis," *IEEE Trans. Computer-Aided Design*, vol. 9, pp. 352–366, Apr. 1990.

57. W. Stillman, M. S. Shur, D. Veksler, S. Rumyantsev, and F. Guarin, "Device loading effects on nonresonant detection of terahertz radiation by silicon MOSFETs," *Electron. Lett.*, vol. 43, no. 7, pp. 422–423, Mar. 2007.